Constraining the variation of fundamental constants with tritium decays

by

Anthony Fradette
B.Sc., McGill University, 2010

A Thesis Submitted in Partial Fulfillment of the
Requirements for the Degree of

MASTER OF SCIENCE

in the Department of Physics and Astronomy

Constraining the variation of fundamental constants with tritium decays

by

Anthony Fradette
B.Sc., McGill University, 2010

Supervisory Committee

Dr. Maxim Pospelov, Supervisor
(Department of Physics and Astronomy)

Dr. Adam Ritz, Departmental Member
(Department of Physics and Astronomy)

Dr. Falk Herwig, Departmental Member
(Department of Physics and Astronomy)

Supervisory Committee

Dr. Maxim Pospelov, Supervisor
(Department of Physics and Astronomy)

Dr. Adam Ritz, Departmental Member
(Department of Physics and Astronomy)

Dr. Falk Herwig, Departmental Member
(Department of Physics and Astronomy)

ABSTRACT

The consistency of fundamental constants is assumed in the Standard Model. However, new physics theories allow them to be dynamical. Different tests can be made at various epochs of the universe. In particular, current bounds at the time of emission of the Cosmic Microwave Background (CMB) permit variations up to 1% of their present values. A change of this order can produce an accumulation of tritium which would later decay and modify the ionization history of the Universe by up to $\mathcal{O}(0.1\%)$. This Tritium Decay Scenario (TDS) can modify the CMB to an observable level and thus provides a new probe of Varying Fundamental Constants (VFC). We analyze the WMAP 7-year and SPT data with respect to the TDS and find no evidence for VFC. The data disfavors a portion of the parameter space at 95% Confidence Level (CL). We forecast the sensitivity of Planck to the TDS and find that a larger range of parameters can be excluded at 3σ CL.

Contents

List of Tables

List of Figures

ACKNOWLEDGEMENTS

There are many people that I need to thank for either their influence, help, support or simply made my life much easier.

The most important on the list is my family. Through their love, education and support, my parents, Diane and Guy, together with my siblings Émilie and Olivier, guided me through life and influenced the personal values that shaped the person I have become.

I would like to thank Dr. Maxim Pospelov for his guidance, support and patience in addition to Dr. Adam Ritz and Dr. Pavel Kovtun for stimulating courses and helpful discussions.

My friends here in the physics department, thank you for interesting conversations (on physics, or not), the fun activities and adventures.

I would like to thank Dr. Julien Lesgourgues and Mr. Benjamin Audren for providing me a pre-release version of MontePython, a computing program critical in my research.

I would like to thank in general the Physics Department at the University of Victoria for providing a stimulating research environment and the Perimeter Institute where early stages of the research in this thesis were done.

DEDICATION

Pour mes parents,
Diane et Guy,
qui me supportent et m'encouragent dans tous mes projets et aventures.

Chapter 1

Introduction

All theories in physics have defining constants, telling us either the strength of the interactions or the scale at which they become relevant. Basic examples are quantum mechanics, where the Planck constant h dictates the level at which quantum effects set in, or special relativity, which is required over classical mechanics for velocities near the speed of light c. Instinctively, these constants have been taken to be *constant* in time and space, hence their name. This is in part due to simplicity (scientists always start with the easiest hypothesis) and the apparent consistency over the years, decades, or centuries even, at ever-increasing precision until the present time.

A rigorous physicist might say that it is part of the scientific method to verify the consistency of fundamental constants and that alone would be enough to motivate the search of Varying Fundamental Constants (VFC). Realistically, the experimental precision will never be infinite and one looses interest at a reasonable point. The recent research effort in VFC [1, 4] is rather due to the potential window on extensions of the Standard Model (SM) or even the *ultimate* physics theory, with string theory as a candidate. Many of these theories allow dynamical fundamental constants, and thus observing the evolution of a SM constant would help us determine the correct extension of our current view of Nature.

The study of cosmology is a great tool to investigate the variation of fundamental constant. The Big Bang theory as been successful at predicting the correct abundances[1] of light nuclei and the existence of a Cosmic Microwave Background (CMB) of photons [1]. It therefore constitutes a strong theoretical basis, with a plethora of fundamental constants incorporated in the microphysics.

[1]Except for ^{7}Li, which observations are 4-5σ lower than predicted [5] and could be an indication of new physics [6].

The CMB is a fossil radiation, emitted when the Universe became transparent. It was first predicted by Gamow [7] indirectly when he used the Hot Big Bang as a means of creating nuclei heavier than ^{1}H and then estimated by Alpher and Herman [8] to ~ 5 K. The isotropic radiation was first famously observed by Penzias and Wilson [9] and its blackbody spectrum was measured with astonishing precision by the COsmic Background Explorer (COBE) satellite [10]. A perfectly homogeneous universe does not allow the genesis of structures through gravitational collapse and small anisotropies of the order $\Delta T/T \simeq 10^{-5}$ were first observed by COBE [11]. The Wilkinson Microwave Anisotropy Probe (WMAP), in conjunction with SPT[2] [12], ACT[3] [13], ACBAR[4] [14], CBI[5] [15], VSA[6] [16] and BOOMERANG[7] [17], refined the measurements of the temperature fluctuations (see figure 1.1) which allowed the extraction cosmological parameters [18].

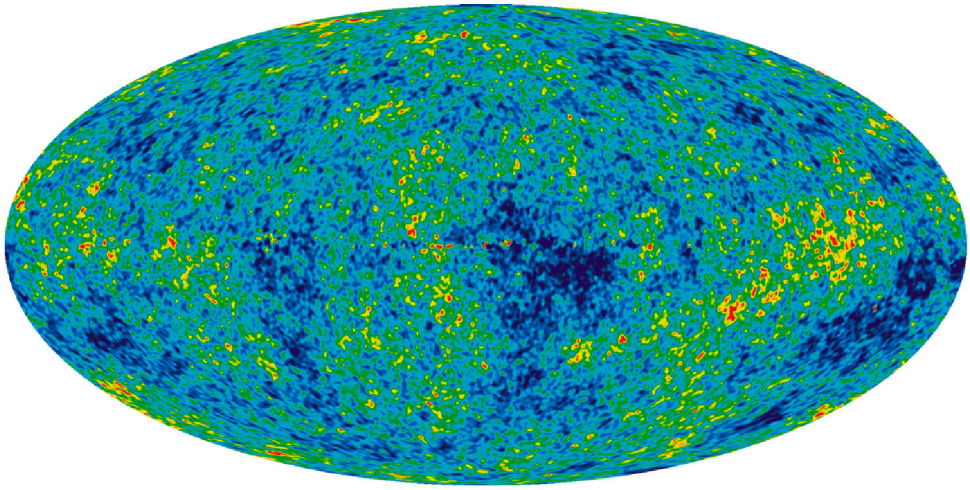

Figure 1.1: Temperature anisotropies in the CMB observed by WMAP. Credit NASA/WMAP Science Team.

The anisotropy power spectra, both in temperature and polarization, are rich sources of information about the Universe. Their characteristic shape of peaks and troughs (see figure 5.1 for the temperature spectrum) are dependent to various de-

[2]South Pole Telescope
[3]Atacama Cosmology Telescope
[4]Arcminute Cosmology Bolometer Array Receiver
[5]Cosmic Background Imaginer
[6]Very Small Array
[7]Balloon Observations Of Millimetric Extragalactic Radiation ANd Geophysics

grees on many parameters. With the current data, a model of the Universe (dubbed ΛCDM) dominated by dark energy and cold dark matter with a nearly scale-invariant spectrum of primordial fluctuations has been established on a strong footing. With the new generation of CMB experiments such as the Planck satellite [19], we are now in an era of *precision cosmology*. The forecast on the data shows that it will set tighter constraints on the cosmological parameters and detail the ionization history, in addition to the possibility of probing inflation physics or deviations from the standard ΛCDM model [19].

In light of this potent cosmological data, we investigate a novel probe of VFC in relation with the CMB. We specifically concentrate on variations of nuclear parameters as there was no previous understanding that the CMB could be sensitive to VFC in the nuclear sector. The allowed variation of constants by present observations can induce a modification in the excess energy Q of the reaction $\mathrm{T} \rightarrow {}^3\mathrm{He} + e^- + \bar{\nu_e}$ in such a way that the stable element in the reaction becomes the tritium atom and the reaction is reversed. The primordial abundance of ^{3}He is then accumulated into T until $Q > 0$. If the sign of Q changes after recombination, the emitted electron in the disintegration of T can partially reionize the Universe which in turn modifies the CMB signal. The Tritium Decay Scenario (TDS) can therefore potentially detect or constraint the evolution of fundamental constants.

The remaining of the thesis is structured as follows.

Chapter 2 is a short review of standard Cosmology, reviewing basic concepts that will be used in the other chapters.

Chapter 3 starts with the motivations behind VFC and its current observational status. We then introduce and discuss the relevance of the Tritium Decay Scenario with respect to the other probes.

Chapter 4 is devoted to the thermal history of the Universe, with a thorough description of its modifications arising from the TDS.

Chapter 5 discusses the CMB and its relation with the background cosmology. We investigate the effects of the modified ionization history.

Chapter 6 is focused on the detectability of the TDS, where CMB data is used to impose constraints on the parameter space. A forecast on the Planck data is also included.

Chapter 7 summarizes our findings and concludes our discussion of the TDS.

Chapter 2

Cosmology Primer

Before we embark into the analysis of varying constants, we review some basic concepts and equations that will be used in other chapters. This will alleviate and smoothen the discussion throughout the Thesis.

2.1 General Relativity

The theory of General Relativity is a geometric interpretation of gravity that preserves Lorentz symmetry. Early after its formulation in 1916 by Albert Einstein, it successfully passed rigorous experimental tests, notably the deviation of light observed by Eddington during a solar eclipse [20]. Its physical implications are entirely encoded in the Einstein equations (see for e.g. [21])

$$R_{\mu\nu} - \frac{1}{2} R g_{\mu\nu} = 8\pi G T_{\mu\nu}, \tag{2.1}$$

where G is Newton's constant. The left-hand side corresponds to the geometry of space, which strictly depends on the line element

$$ds^2 = g_{\mu\nu} dx^\mu dx^\nu, \tag{2.2}$$

from which we can extract the metric $g_{\mu\nu}$ of the background. The Ricci tensor $R_{\mu\nu}$ and the Ricci scalar R are defined by

$$R_{\mu\nu} = \partial_\alpha \Gamma^\alpha_{\mu\nu} - \partial_\nu \Gamma^\alpha_{\mu\alpha} + \Gamma^\alpha_{\beta\alpha}\Gamma^\beta_{\mu\nu} - \Gamma^\alpha_{\beta\nu}\Gamma^\beta_{\mu\alpha} \tag{2.3}$$

$$R = g^{\mu\nu} R_{\mu\nu} \tag{2.4}$$

with the Christoffel symbols given by

$$\Gamma^{\lambda}_{\mu\nu} = \frac{g^{\lambda\sigma}}{2}\left(\partial_\mu g_{\nu\sigma} + \partial_\nu g_{\sigma\mu} - \partial_\sigma g_{\mu\nu}\right) \tag{2.5}$$

The right-hand side of 2.1 is sourced by the stress-energy tensor $T_{\mu\nu}$, which describes the energy constituents filling the universe. For a perfect isotropic fluid, the general form is

$$T^{\mu\nu} = (\rho + p)U^\mu U^\nu + p g^{\mu\nu}, \tag{2.6}$$

where ρ is the energy density, p the pressure and $U^\mu = \frac{dx^u}{d\tau}$ is the four-velocity, with proper time τ. The Einstein equations therefore relate the content of a spacetime with its geometry.

2.2 Friedmann Equations

We know from Hubble that the universe is expanding. Assuming spatial isotropy and homogeneity, one can study a smoothly expanding universe with the Robertson-Walker metric

$$ds^2 = -dt^2 + a^2(t)\left[\frac{dr^2}{1-\kappa r^2} + r^2 d\Omega^2\right]. \tag{2.7}$$

The scale factor a represents the relative physical distance. The coordinates $\vec{r}$ are comoving with the expansion, meaning that objects fixed on the comoving grid at a distance d now were separated by $a(t)d$ at time t. This implies the normalization $a_0 \equiv a(t_{\rm now}) = 1$, where the subscript 0 will denote the present time throughout this Thesis. The curvature parameter κ quantifies the behaviour of parallel lines. If $\kappa < 0$ the distance between two locally parallel lines will diverge at infinity and the universe is said to be open. Conversely, if they converge the universe is closed and $\kappa > 0$. Present observations suggest our universe is very nearly flat [22], and for simplicity we will assume $\kappa = 0$ for the remainder of this manuscript.

The evolution of the scale factor is embedded in Einstein equations, and its reduced form is known as the Friedmann equations

$$H^2 = \frac{8\pi G}{3}\rho \tag{2.8}$$

$$\frac{\ddot{a}}{a} = -\frac{4\pi G}{3}(\rho + 3p), \tag{2.9}$$

where we have defined the Hubble parameter $H = \frac{\dot{a}}{a}$. If the universe is filled with different types of energy, $\rho = \sum_i \rho_i$. In the standard ΛCDM cosmology, all types of energy follow the equation of state $p_i = w_i \rho_i$, where w_i is constant and defines the type of energy. The three standard form of energy are matter ($w_m = 0$), radiation ($w_r = \frac{1}{3}$) and vacuum ($w_\Lambda = -1$). The time-dependence of each ρ_i is found through the conservation of $T_{\mu\nu}$ which implies

$$\rho_i = \rho_{i0} a^{-3(1+w_i)}. \tag{2.10}$$

We therefore have a closed system of equations to track the evolution of the scale factor and the energy densities. We show in figure 2.1 the fractional amount of energy density $\Omega_i = \frac{\rho_i}{\rho_{\text{tot}}}$ as a function of the scale factor, clearly demonstrating that the universe is dominated by different types of energy at different epochs.

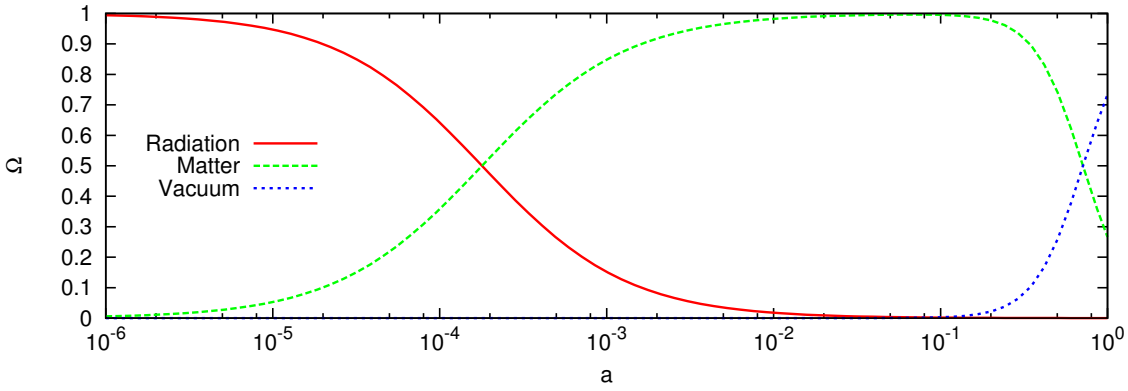

Figure 2.1: Evolution of the cosmic energy distribution.

2.3 Cosmological Distances and Time

There are many different ways we can parametrize the cosmological evolution. The scale factor a dictates the evolution of energy densities and tells us the relative separation between objects on the comoving grid. We can map the size of the universe to the physical time by integrating 2.8

$$t = \int_0^a \frac{da}{\sqrt{\frac{8\pi G}{3} a^2 \rho}}, \tag{2.11}$$

where we have taken $a(0) = 0$. Recalling the normalization $a_0 = 1$, it is convenient to define another variable z

$$a = \frac{1}{1+z}. \tag{2.12}$$

When light travels through spacetime, its wavelength is redshifted as space expands by $\frac{\lambda_{\rm obs}}{\lambda(a)} = \frac{1}{a}$. The fractional change is $\frac{\Delta\lambda}{\lambda_{\rm emit}} = z$ and for this reason we call z the redshift.

Another useful quantity is the maximal distance a photon could have traveled in a given time, therefore defining the size of the light-cone of a past event. In terms of comoving coordinates, we defined the conformal time from the Big Bang

$$\eta = \int_0^t \frac{dt'}{a(t')}. \tag{2.13}$$

As the universe expands, wavelengths are stretched and the temperature scales linearly with the scale factor. We can thus specify any cosmological epoch by the radiation temperature

$$T(z) = (1+z)T_0, \tag{2.14}$$

where $T_0 = 2.726$ K, the present-day temperature of the radiation relic.

Chapter 3

Dynamical Fundamental Constants

The idea of Varying Fundamental Constants (VFC) was first suggested by Dirac in 1937 [23]. He noticed that characteristic dimensionless numbers such as the ratio between the electrostatic and gravitational force between an electron and a proton

$$\frac{F_{em}}{F_g} = \frac{e^2}{Gm_p m_e} \simeq 2 \times 10^{39} \tag{3.1}$$

or the ratio of the Hubble radius over the classical radius of the electron

$$\frac{r_H}{r_e} = \frac{cH_0^{-1}}{e^2 m_e^{-1} c^{-2}} \simeq 5 \times 10^{40} \tag{3.2}$$

lie in the same range of orders of magnitude. He postulated that this numerical coincidence had a deeper meaning, summarized in his own words [24]

> *Any two of the very large dimensionless numbers occurring in Nature are connected by a simple mathematical relation, in which the coefficients are of the order of magnitude unity.*

Since the Hubble rate evolves in time (see 2.8), it would imply that constants involved in either 3.1 or 3.2 change through the different epochs of the universe.

This numerological source of VFC was not based on very scientific grounds, but the concept was nonetheless introduced in the academic literature. Nowadays, VFC are seen as a possible window on New Physics and constitutes a complete research field, both theoretical and experimental. In this chapter, we review these advancements to justify and introduce a new probe of VFC.

3.1 Theories with varying constants

Although we are only interested in a phenomenological study of VFC, it is important to briefly review some theoretical work that justifies its physical realizations.

The first implementation of VFC in a field-theory framework was done by Jordan [25], where he considered G to be a dynamical field. The idea was extended by Brans and Dicke [26] and then generalized into scalar-tensor theories of gravity. The idea is that gravity is not only mediated by a spin-2 graviton, but also by a scalar field that couples universally to matter fields [1]. This coupling can affect particle physics, notably induce a time-evolution of the fine-structure constant through quantum effects [27].

Alternatively, it was shown by Bekenstein [28] that the electromagnetic sector of the Standard Model can be modified to incorporate a dynamical evolution of the fine-structure constant. He noticed that radiation cannot source a variation in $\alpha_{\rm em}$. Rather, its temporal evolution is driven by the baryon energy density and is thus relevant on cosmic scales. The model has more recently been generalized with couplings to the currently dominating energy densities, dark matter and dark energy, allowing greater variations in $\alpha_{\rm em}$ [29].

A general feature of string theory is the presence of the dilaton, a scalar field. According to this candidate description of quantum gravity, the values of different couplings and masses in the standard model are derived from the vacuum expectation value of the dilatons [30], which could change on cosmological scales, provided that the dilaton remains nearly massless.

These three examples certainly do not form an exhaustive list of theoretical frameworks of VFC. Instead, they are meant to demonstrate that there are many ways to incorporate VFC in the current picture of particle physics and cosmology. An experimental proof of VFC would then guide us in the determination of the correct extension of the Standard Model.

The variation of Standard Model constants is generically driven by a new dynamical field. In this thesis, we neglect the effects of the field stress-energy tensor on the cosmology, and only consider the implications of the induced VFC.

3.2 Current constraints

Ideally, knowing the evolution function of the fundamental constants through all redshifts would give us maximal information about the VFC. However, since their evolution is only detectable indirectly in different physical processes with various sensitivity, we can only hope to patch enough measurements to track the evolution over the different cosmological epochs.

We briefly review the known physical systems that provide constraints starting from present bounds going back in time, summarized with their order of magnitude constraint in table 3.1 (for recent reviews, see for e.g. [1, 4]).

Atomic clocks allow present-day constraints by comparing the frequency of ultra-stable oscillators in different elements. For example, the SI second is defined by the cesium hyperfine transition [31] which can be compared with the magnesium fine structure transition to probe the variation of α [32].

The Oklo phenomenon corresponds to an uranium mine that had natural nuclear reactors that operated approximately 2 billion years ago in the town of Oklo, Gabon. It left peculiar distributions of some isotopes around the mine, from which we can extract information about the reaction rates and learn about the fundamental constants at the time [33].

Meteorite dating can be used to look at the concentrations of long-lived radioactive elements, affected by α- or β-decay. The integrated decay rate can be found, thus constraining the evolution of α_{em} [34].

Quasar Spectra offer another possibility of observing the variation of fundamental constants. By looking at the chromatic effects not accounted by redshift in the absorption lines, one can constrain their evolution [35].

Stellar physics provides rigid bounds by requiring the proper abundance of carbon produced through nucleosynthesis in the stellar cores [36, 37].

The 21 cm absorption line from ground state hyperfine splitting of neutral hydrogen in the IGM probes the universe at different redshifts during the dark ages. Its details can potentially map the evolution of fundamental constants through a large range of redshifts [38].

The CMB is a picture of the universe when it became neutral. Changes in $\alpha_{\rm em}$ and m_e mostly affect the recombination process, which modifies the optical depth. The effect is large enough to limit the variations of constants at this epoch [39].

Big Bang Nucleosynthesis (BBN) is the name given to the system of nuclear reactions through which the light elements are created in the early universe. The final abundances are dominantly sensitive to the mass difference between the proton and the neutron in addition to the deuteron binding energy, which can be related to fundamental constants [40].

Redshift	System	Observable	Constraint Order $[10^X]$
Now	Atomic clock	frequency change	-17^*
0.14	Oklo phenomenon	isotopic ratio	-7
0.43	Meteorite dating	isotopic ratio	-7
0.2-4	Quasar spectra	atomic spectra	-5
15	Stellar physics	element abundances	-3
30-100	21 cm	$T_b/T_{\rm CMB}$	-3
1000	CMB	$\Delta T/T$	-2
10^8	BBN	light element abundance	-2

Table 3.1: Summary of the different probes of variation of fundamental constants. The constraint order is the order of magnitude of the allowed fractional difference $\left|\frac{\alpha_z-\alpha}{\alpha}\right|$ between the redshift z and now. * Atomic clocks bounds are on the yearly fractional change, $\left|\frac{\dot{\alpha}}{\alpha}\right| < 10^{-17}{\rm yr}^{-1}$. Data from [1].

3.2.1 Detection controversy

It is important to point that all measurements are consistent with no change in fundamental constants, except limits from quasar absorption lines. Webb *et al.* claimed a detection of smaller $\alpha_{\rm em}$ at 4.7σ [41] using data from HIRES (HIgh Resolution Echelle Spectrometer) on the Keck telescope. The same authors, with a larger collaboration, analyzed the data from ESO Very Large Telescope (VLT) and noticed the *opposite* feature, a larger $\alpha_{\rm em}$ [42]. Since Keck/HIRES and VLT observe different portions of the sky, they claimed a spatial dipole variation of $\alpha_{\rm em}$, significant at the 4.2σ level [42]. In Ref. [43], the authors analyzed the data accuracy of Keck/HIRES and argue that it is difficult to claim a variation of fundamental constants. Ref. [44] reanalyzed the updated dataset from both Keck and VLT telescopes, mentioning that they could

not find any systematic effect that would account for the spatial dipole variation of $\alpha_{\rm em}$. Finally, Ref. [45] recently demonstrated through a Bayesian reanalysis that, with our current theoretical and observational knowledge, no definitive conclusions can be reached and more independent data is required to settle the debate.

3.2.2 CMB constraints

The temperature anisotropies in the CMB (see chapter 5 for an overview of the CMB physics) are an artifact of the primordial quantum density fluctuations, which are the seeds for the gravitation collapse and creation of celestial bodies. The perturbations in the photon energy distribution are sourced by the Compton coupling with the ionized matter and the redshifting (blueshifting) when the photon comes out of an under-densed (over-densed) gravitational potential well.

The evolution of the temperature fluctuations is described by the Boltzmann equation 5.9. The Compton interaction is proportional to the differential optical depth $\dot{\kappa}$

$$\dot{\kappa} = X_e n_e \sigma_T, \tag{3.3}$$

where X_e is the ionized fraction of matter, n_e the electron number density and σ_T the Thomson cross section. The effect of varying $\alpha_{\rm em}$ or m_e on the anisotropies is dominated by the change it induces in $\dot{\kappa}$ [39]. Factoring out the dilution from space expansion, the electron number density is fixed. The effect on σ_T is easily seen by writing out its definition

$$\sigma_T = \frac{8\pi}{3}\frac{\alpha_{\rm em}^2}{m_e^2}. \tag{3.4}$$

The evolution of X_e is solved through a system of differential equations described in section 4.2.1, following the rates of recombination and ionization. Qualitatively, increasing $\alpha_{\rm em}$ augments the binding energies, which yields a faster and earlier recombination of the medium [46].

This probe of VC has been investigated by many authors, with increasing precision and updated datasets [47, 48, 49, 50, 51, 52, 53]. We would like to point out that in all analyses, the authors simply varied $\alpha_{\rm em}$ in all its occurrences in the numerical codes and *did not consider new physics affecting the recombination process.*

3.3 A Novel Effect

We propose a new mechanism triggered by VFC that has non-negligible implications in the recombination of the cosmic medium and the CMB. As will be explained in section 4.1, light elements are formed in the early Universe and the final abundances are the result of a network of nuclear reactions. In particular, Tritium (T) decays into Helium-3 (^{3}He). According to the SM, this decay happens very quickly ($\tau_{1/2} = 12.32$ years) on cosmological timescales and T is entirely depleted at recombination (~ 300000 years later). The interesting feature is the excess energy Q of the reaction

$$Q = m_{\mathrm{T}} - m_{^3\mathrm{He}^+} - m_e = 18.59 \text{ keV} \tag{3.5}$$

where the neutrino mass is negligible. It is notably small compared to the mass of the parent atom.

$$\frac{Q}{m_{\mathrm{T}}} \sim 6.7 \times 10^{-6} \tag{3.6}$$

We can therefore expect that fundamental constants involved in m_{T} and $m_{^3\mathrm{He}}$ can have sizable effects on the excess energy. The new probe of VFC can be stated as

> If the VFC influences Q in such a way that it is negative, the primordial ^{3}He decays into the stable tritium. At some point, Q must become positive and reach its SM value. If the transition happens around the last-scattering surface, the belated beta decay of the accumulated tritium then injects energy in the cosmic medium through kinetic electrons, altering the recombination process and partially reionizing the Universe.

Multiple fundamental constants influence the value of Q. Keeping the current observational status in mind, we highlight some of them that can realistically give rise to the Tritium Decay Scenario (TDS).

3.3.1 Variation in α_{em}

We can estimate the required variation in the fine-structure constant to obtain $Q < 0$. In general, the mass of an atom with A nucleons and Z protons is given by

$$m(A, Z) = Zm_p + (A - Z)m_n + Zm_e + E_s + E_{em}, \tag{3.7}$$

where E_s and E_{em} are respectively the strong and electromagnetic contributions to the binding energy. A semi-empirical approximation of the binding energy is given by the Bethe-Weiszäcker formula [54], from which we can extract the nuclear E_{em} term [1]

$$E_{em} = 98.25 \frac{Z(Z-1)}{A^{\frac{1}{3}}} \alpha_{\rm em} \text{ MeV}. \tag{3.8}$$

Moreover, the nucleons are made of quarks which are charged under electromagnetism. Their masses therefore have an implicit dependence on $\alpha_{\rm em}$. Concretely, we can be expand their mass at lowest order in chiral perturbation theory as [55]

$$m_{(p,n)} = A + b_{(u,d)} m_u + b_{(d,u)} m_d + B_{(p,n)} \alpha_{\rm em}, \tag{3.9}$$

where A is the pure QCD contribution and $b_{(u,d)}$ are the quarks' quadratic expectation values in the proton $b_q = \langle p|\bar{q}q|p\rangle$. The electromagnetic self-energy contribution as been theoretically calculated in the context of n/p mass difference [56]

$$(B_p - B_n)\alpha_{\rm em} = 1.30 \pm 0.50 \text{ MeV}. \tag{3.10}$$

Neglecting the effect of the strong force between the nucleons, we can write the nuclear part of the excess energy as

$$Q^{\rm nuc} = m_{\rm T}^{\rm nuc} - m_{^3{\rm He}}^{\rm nuc} = (b_d - b_u)(m_u - m_d) - 314.4\alpha_{\rm em} \text{ MeV}. \tag{3.11}$$

The TDS can therefore be achieved with an increase of

$$\frac{\Delta\alpha_{\rm em}}{\alpha_{\rm em}} \simeq 10^{-2}, \tag{3.12}$$

a variation at the same order of the current constraints.

3.3.2 Variation in masses

Another possibility is a change in the mass of the nucleons and the electron. Although not fundamental (see eq. 3.9), we consider nucleon masses as the varying parameters. Using 3.7, we write Q as

$$Q = m_n - m_p + E_{^3{\rm He}^+} - E_{\rm T} - m_e + \delta E^{\rm nuc}, \tag{3.13}$$

where E_x is the binding energy of the orbiting electron and δE^{nuc} the difference between the two nuclear binding energies. The electromagnetic binding energy is given by the standard $E = \frac{m_e \alpha^2 Z^2}{2}$ and is negligibly small compared to the rest masses. The expression then reduces to

$$Q = m_n - m_p - m_e + \Delta E^{\text{nuc}}. \tag{3.14}$$

The required independent variations are therefore

$$\frac{\Delta(m_n - m_p)}{m_n - m_p} \simeq -0.015 \qquad \frac{\Delta m_e}{m_e} \simeq 0.04. \tag{3.15}$$

We show as an example of joint variations the contour lines of the excess energy when the nucleon masses and the fine-structure constant are both allowed to vary in figure 3.1. The shaded region marks the parameter space where tritium is stable and $Q < 0$.

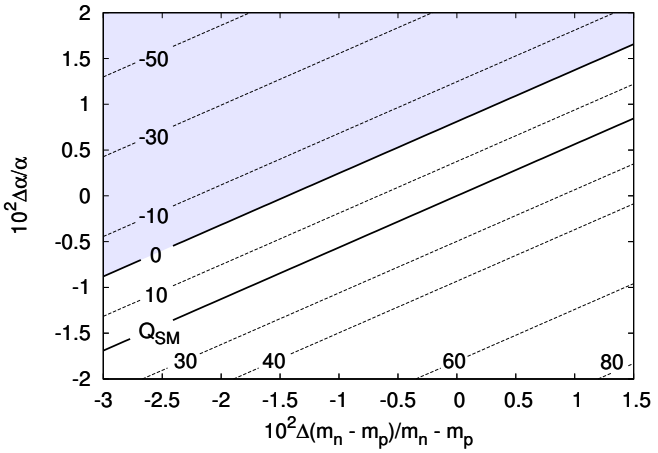

Figure 3.1: Contour lines of Q in keV for a variation in the nucleon masses and the fine-structure constant. The shaded region allows a negative Q.

3.4 Modeling the variation

Having justified the possible realization of TDS through different varying constants channels, we can quantify the impact of a time-varying Q in the tritium decays.

3.4.1 Tritium → Helium-3

In the Standard Model, tritium T naturally decays into ^{3}He through beta decay with and half-life of $t_{\frac{1}{2}} = 12.32$ years. The Feynman diagram of the reaction is shown in figure 3.2. We generalize (see appendix A for details) the decay rate Γ to a variable excess energy Q

$$\Gamma_{\mathrm{T}\to\mathrm{He}}(Q) = \frac{(G_F V_{ud})^2}{2\pi^3}(g_v^2 + 3g_a^2)\int_{m_e}^{m_e+Q} \mathrm{d}E\, F(2,E)E\sqrt{E^2 - m_e^2}(Q + m_e - E)^2, \tag{3.16}$$

where the integral is over E, the outgoing electron energy that we have approximated to be non-relativistic. $F(2,E)$ is the Coulomb correction factor [57] that incorporates the electromagnetic interaction between the $^3\mathrm{He}^+$ and the electron. The Fermi constant $G_F = 1.16637(\hbar c)^3 10^{-5}$ GeV^{-2} and CKM matrix element $V_{ud} = 0.97425$ are set at their respective Standard model values [3]. By the Conserved Vector Current hypothesis, we set the vector coupling $g_v = 1$. The axial coupling $g_a = 1.239$ is found numerically by equating the left-hand side of 3.16 for $Q = Q_{sm} = 18.59$ keV with the Standard Model decay rate $\Gamma = 1.783$ nHz. It is close to g_a from the β-decay of free neutrons.

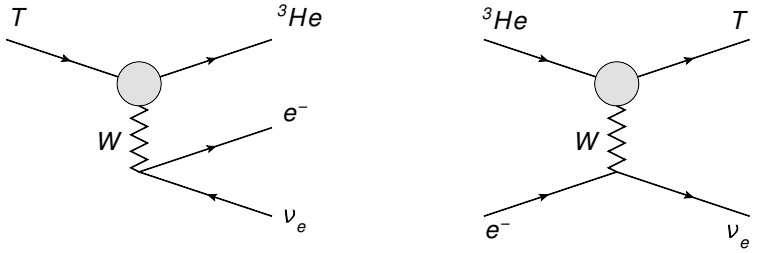

Figure 3.2: Feynman diagrams of the reactions T $\rightleftarrows$ ^{3}He.

The non-trivial nature of $F(2,Z)$ (see A.11) makes it difficult to find an analytic solution to 3.16 and we have to settle with a numerical solution. We found that it could be well-fitted with a polynomial of the form

$$\Gamma_{\mathrm{T}\to\mathrm{He}}(Q) = aQ^3 + bQ^4 + cQ^5 + dQ^6 + eQ^7, \tag{3.17}$$

where the coefficient values are given in table 3.2 and Q is in eV. The numerical and fitted solutions are shown in figure 3.3 and differ by at most 1.6% for small Q where $F(2,E)$ has a greater impact. For $Q > 10$ keV, they differ by $\mathcal{O}(0.001\%)$.

	a	b	c	d	e
$\Gamma(Q)$	1.4169×10^{-22}	1.1489×10^{-26}	-3.9029×10^{-31}	1.1909×10^{-35}	-1.6235×10^{-40}
$K(Q)$	0.2559	9.0211×10^{-6}	-7.8795×10^{-10}	3.6221×10^{-14}	-6.5085×10^{-19}

Table 3.2: Fitting parameters of the curves in figure 3.3 modeled as 3.17 and 3.18 for respectively the decay rate of tritium Γ and the average kinetic energy of the ejected electron K.

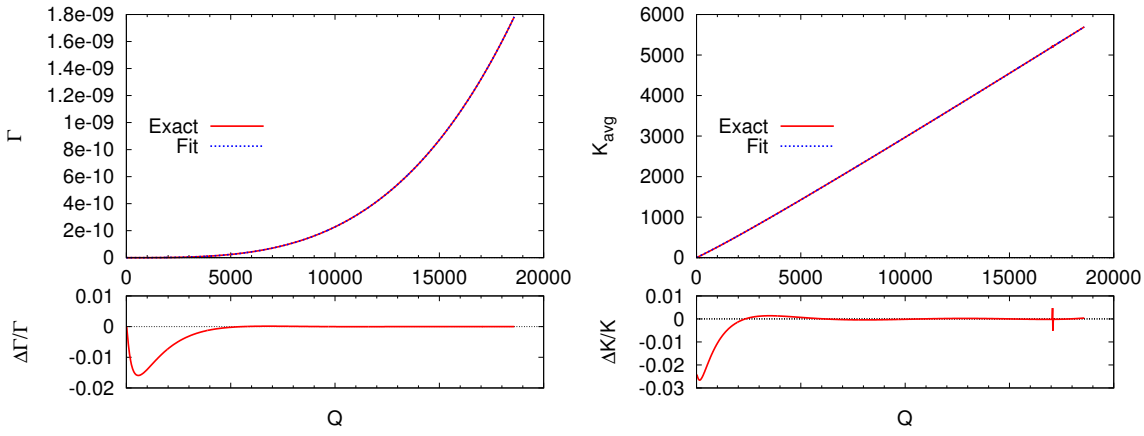

Figure 3.3: Tritium decay rate and average kinetic energy of the electron emitted as a function of the excess energy Q in eV.

The decay has three products and since $m_{^3\mathrm{He}} \gg m_{e,\nu}$, we can take the rest frame of the decaying tritium to be same as the ^{3}He product. Then, all the kinetic energy will be distributed between the electron and the neutrino. The energy distribution of the electron is given by the integrand in 3.16 and the average kinetic energy of the electron K_e is given by

$$K_e(Q) = \frac{\int_{m_e}^{m_e+Q} \mathrm{d}E\, F(2,E) E^2 \sqrt{E^2 - m_e^2}(Q + m_e - E)^2}{\int_{m_e}^{m_e+Q} \mathrm{d}E\, F(2,E) E \sqrt{E^2 - m_e^2}(Q + m_e - E)^2} - m_e. \tag{3.18}$$

The numerical solution and fit with the polynomial

$$K_e(Q) = aQ + bQ^2 + cQ^3 + dQ^4 + eQ^5 \tag{3.19}$$

are shown in figure 3.3 and the coefficients listed in table 3.2. The polynomial differs by 3% or less for small Q and for $Q > 10$ keV they agree at the 0.05% level.

3.4.2 Helium-3 → Tritium

For completeness, we derive (see A.2) the rate of the ^{3}He to T decay shown in figure 3.2. The process happens through the electron capture of one of the orbiting electrons and we find

$$\Gamma_{\mathrm{He}\to\mathrm{T}}(\tilde{Q}) = \frac{3\cdot 10.572}{8\pi^2}\frac{G_F^2 V_{ud}^2}{\alpha c}\tilde{Q}^2(g_v^2+3g_a^2)\frac{\mathrm{MHz}}{\mathrm{fm}^2}, \tag{3.20}$$

where we assumed the initial T, electron and final ^{3}He to be at rest. We stress the fact that this reaction is only possible for *negative* Q-values with respect to the opposite reaction. We rename $\tilde{Q} = -Q > 0$ to make a clear distinction between the two cases.

This decay rate corresponds to a lifetime of

$$\tau_{\mathrm{He}\to\mathrm{T}}(\tilde{Q}) = 2.05\times 10^5\,\mathrm{yr}\left(\frac{10\,\mathrm{keV}}{\tilde{Q}}\right)^2. \tag{3.21}$$

3.4.3 Time evolution of Q

To model the evolution of Q, we take the simplest polynomial that smoothly transitions from 0 to Q_{sm} with vanishing first and second derivatives at those points. Writing the time-dependence in redshift z, we have two free parameters, the redshift z_0 at which Q becomes positive and the timescale Δz of the transition to Q_{sm}. The evolution of the excess energy is then given by

$$Q(z) = Q_{sm}\times\begin{cases} 0 & z\geq z_0 \\ 10\left(\frac{z_0-z}{\Delta z}\right)^3 - 15\left(\frac{z_0-z}{\Delta z}\right)^4 + 6\left(\frac{z_0-z}{\Delta z}\right)^5 & 0<\frac{z_0-z}{\Delta z}<1 \\ 1 & z_0-z\geq\Delta z \end{cases} \tag{3.22}$$

and is shown in figure 3.4. The requirement of vanishing first and second derivatives at the transition endpoints becomes helpful in the numerical computation of the cosmological anisotropy spectra. Realistically, we need $Q<0$ at earlier times to convert the primordial ^{3}He into T. In practice, the period where Q is negative does not have other phenomenological effects and the observables only depend on positive Q, provided that all primordial ^{3}He has decayed into T before the transitional epoch z_0. Our model 3.22 serves as an ansatz in our phenomenological study. A dynamical model of VFC is needed to derive a more specific expression for $Q(z)$, but our ansatz should provide enough information to test the detectability of the TDS.

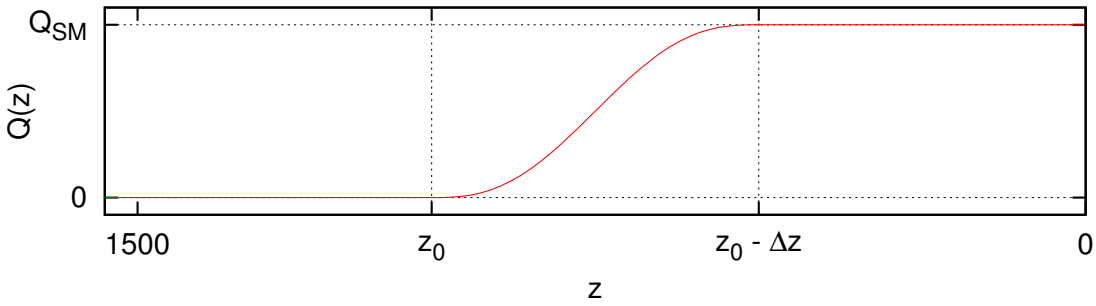

Figure 3.4: Time-evolution model of the excess energy Q in tritium beta-decay

Chapter 4

Thermal History of the Universe

The universe evolves in time; the planets, stars and galaxies formed through gravitational collapse and their chemical composition is the result of chains of multiple reactions. In fact, there are many specific epochs where the composition of the universe changed and the outcome of each transition serves as the initial conditions for the following one, thus influencing the present visible universe.

In this chapter, we review the different phases of the Universe and thoroughly quantify the effects of the TDS in this thermal history.

In its earliest moments, the universe is very hot and dense. The scattering rates between the particles are much larger than the expansion rate, thus enforcing chemical equilibrium. As the temperature cools down, the efficiency of certain processes is lowered and particle distributions are altered. Starting at experimentally tested energies to argue with a certain confidence, we highlight the most relevant transitions.

When the universe is about 10^{-10} second old, the temperature falls under 1 TeV and approaches the Higgs field vacuum expectation value of 246 GeV. As the energy drops under 100 GeV, the weak interaction strength is significantly reduced and its force carriers, the Z and $W^{\pm}$ bosons gain mass through electroweak symmetry breaking. The cross section is still large enough to keep the neutrinos in thermal equilibrium until 1 second has passed and the ambient temperature is around 1 MeV. [58]

Meanwhile, free quarks start to combine and form the first baryons at a temperature of 100 MeV, corresponding to 10^{-4} second. It is worth noting that this temperature is significantly lower than the rest mass energy of ~ 1 GeV. At earlier times, the high-energy tail of the photon distribution is significant enough to destroy any baryons because of the high ratio of photon-to-baryon ($\sim 10^{10}$). Neutrons and protons are kept in equilibrium through the weak force until the temperature is

around 1 MeV. [59] Up until this stage, there are no direct observational probes of the hot Universe until the temperature reaches a few MeV.

4.1 Big Bang Nucleosynthesis

Eventually, the free protons and neutrons join through the strong force to form light elements, a process called Big Bang Nucleosynsthesis (BBN). The main product is ^{4}He since its binding energy of ~ 28 MeV corresponds to the local maximum for the light elements in the distribution of binding energies. The final abundances depend on the relative number of neutrons to protons prior to nucleosynthesis. The relevant weak interactions between the free neutrons and protons are

$$n + \nu_e \rightleftarrows p + e^- \qquad , \qquad n + e^+ \rightleftarrows p + \bar{\nu_e}. \tag{4.1}$$

The interaction rates become smaller than the expansion rate at $T_{\text{freeze}} \simeq 0.84$ MeV and the neutron fraction freezes out to $X_n \equiv \frac{n_n}{n_n+n_p} \simeq 0.158$. At this point, the allowed neutron decay

$$n \to p + e^- + \bar{\nu_e} \tag{4.2}$$

had been irrelevant since the neutron lifetime if $\tau_n \simeq 886\,\text{s} \gg t_{\text{freeze}} \sim \mathcal{O}(1)$ s. However, BBN starts when $t \sim 250$ s and thus the neutron fraction is reduces to $X_n \simeq 0.12$. Since ^{4}He is the local maximum in binding energy for the light elements, it corresponds to the lowest energy state and therefore its abundance will be maximized. Nearly all neutrons will end up in ^{4}He, yielding a relative abundance by mass of

$$Y_p \equiv \frac{m_{^4\text{He}} n_{^4\text{He}}}{m_b n_b} = 2X_n \simeq 0.25, \tag{4.3}$$

since $n_{^4\text{He}} \simeq \frac{n_n}{2}$ and $n_b = n_n + n_p$. Only traces of other light elements are synthesized.

To obtain the exact abundances, one needs to solve the Boltzmann equation (see Appendix B) for each species of nuclei. In theory, all nuclei should be included and one would need to solve a large system of coupled differential equations. In practice, elements heavier than ^{7}Li can be neglected and the relevant reactions are shown in figure 4.1. This simplification is allowed because the lightest element having a larger binding energy than ^{4}He is carbon ^{12}C, synthesized through the reaction

$$^4\text{H} + {}^4\text{He} + {}^4\text{He} \to {}^{12}\text{C}, \tag{4.4}$$

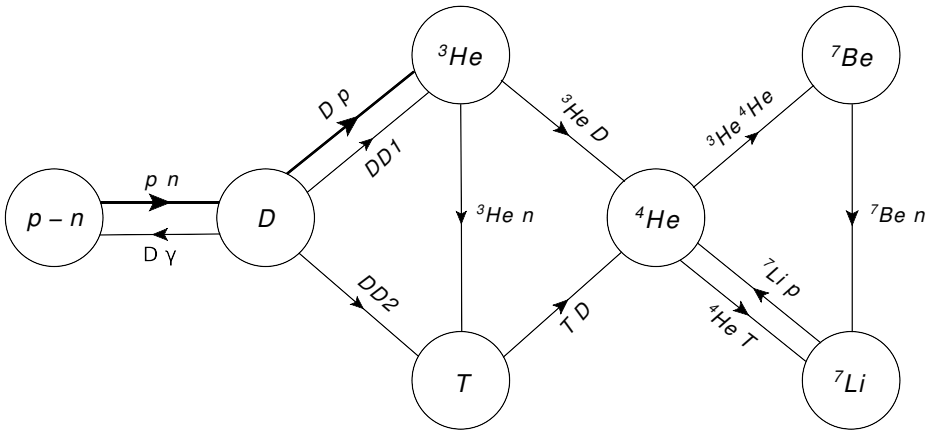

Figure 4.1: Main reactions in BBN. Each line is labeled by the reactants. $DD1$ corresponds to $D + D \rightarrow^3 He + n$ and $DD2$ to $D + D \rightarrow T + p$. Inspired by [2].

which is highly suppressed due to the low number density of the reactants, thus dwarfing the 3-body cross section. The heavier elements will be created in stars, where the density formed by gravitational collapse become high enough to allow 4.4 at a decent rate.

This system has been solved numerically in ref. [60] and is shown in figure 4.2a. It is standard to state the abundance of ^{4}He as Y_p, the mass fraction relative to the total mass of baryons. Its actual relative number density by nuclei is $f_{He} \equiv \frac{n_{^4\mathrm{He}}}{n_H} = \frac{Y_p}{4-Y_p} \simeq 0.07$. All other species abundances are quoted as their relative number density to the hydrogen nuclei. BBN has only one free parameter $\eta_\mathrm{B} = \frac{n_\mathrm{B}}{n_\gamma}$, which is determined by the WMAP satellite. In particular, with a baryon to photon ratio of $\eta_B = 6.2 \times 10^{-10}$ from WMAP5 [61], the abundance of ^{3}He and T are

$$\left.\frac{^3\mathrm{He}}{\mathrm{H}}\right|_p = 1.00 \times 10^{-5}, \qquad \left.\frac{\mathrm{T}}{\mathrm{H}}\right|_p = 7.8 \times 10^{-8}. \tag{4.5}$$

4.1.1 The Tritium Decay Scenario in BBN

Ultimately, we want to analyze the effects of the TDS on the CMB radiation. Since the Universe is opaque at the BBN epoch, the outcome of the primordial nucleosynthesis serves as initial conditions on CMB physics. Therefore, for the TDS to be viable, we must verify that it does not spoil BBN. We consider the three variation channels proposed in section 3.3.

The fundamental constants enter everywhere in the network of differential equa-

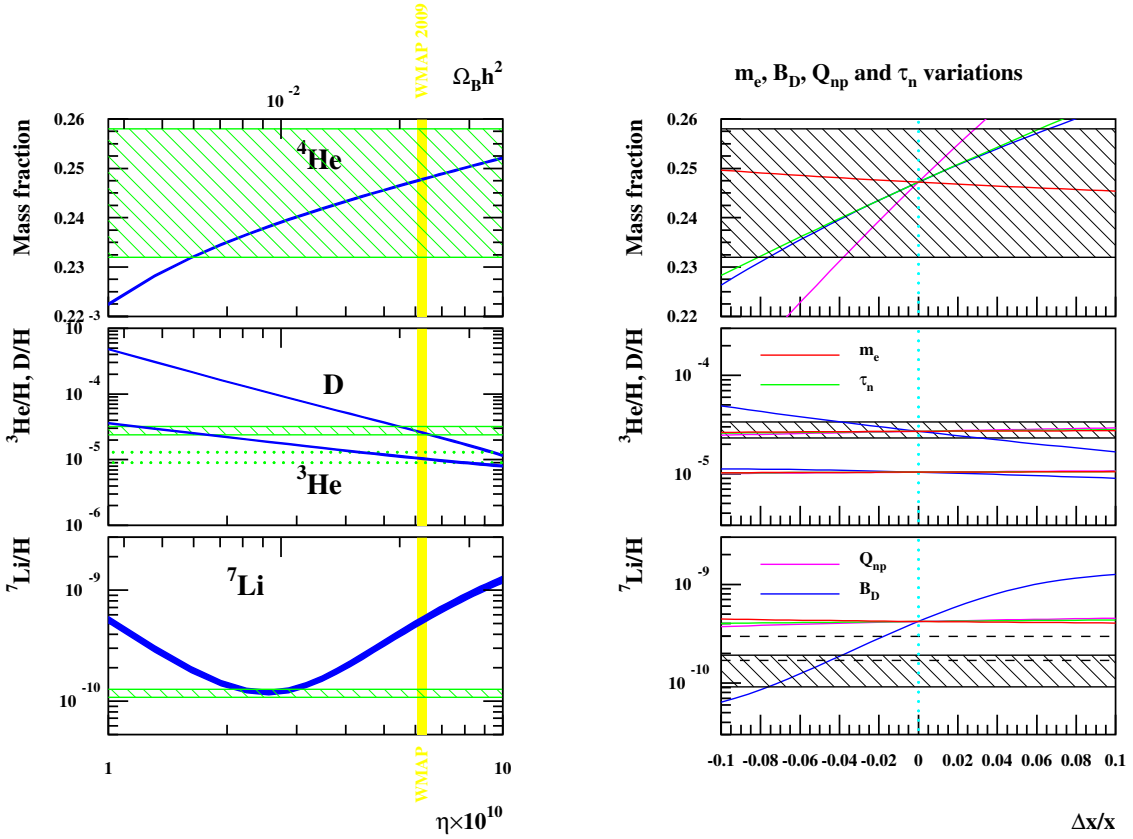

(a) The BBN abundances predictions are fixed by η which is measured by WMAP.

(b) Dependencies of the independent variation of certain parameters.

Figure 4.2: BBN dependencies on different parameters. Uncertainty in observed abundances are represented by the dashed regions. Reproduced from [1].

tions governing the nuclear reactions and tracking the effects precisely is only possible numerically. We can however look at the initial conditions, namely neutron-proton ratio before deuterium starts to form. Since they are in equilibrium prior their freeze-out, we can estimate the behaviour with

$$\left.\frac{n}{p}\right|_f \simeq \mathrm{e}^{-\frac{Q_{np}}{T_f}}, \tag{4.6}$$

where $Q_{np} = m_n - m_p$ and T_f is set to match the correct freeze-out fraction. Including the neutron decay, the ^{4}He mass abundance is then approximately

$$Y_p \sim 2\frac{1}{1+\mathrm{e}^{\frac{Q_{np}}{T_f}}}\mathrm{e}^{-\frac{t_N}{\tau_n}}, \tag{4.7}$$

where t_N is the nucleosynthesis starting cosmic time and τ_n the neutron lifetime. We can linearize the variation effects of these 4 parameters to get

$$\frac{\Delta Y_p}{Y_p} \simeq 0.3 \left(-\frac{\Delta Q_{np}}{Q_{np}} + \frac{\Delta T_f}{T_f} - \frac{\Delta t_N}{t_N} + \frac{\Delta \tau_n}{\tau_n} \right). \tag{4.8}$$

It is important to point out that these parameters have inter-dependencies, for example the lifetime of the neutron can be written as [62]

$$\tau_n^{-1} = \frac{1+3g_A^2}{120\pi^3} G_F^2 m_e^5 \left[\sqrt{q^2-1}(2q^4 - 9q^2 - 8) + 15q \ln\left(q + \sqrt{q^2-1} \right) \right] \tag{4.9}$$

where $q = Q_{np}/m_e$, so that

$$\frac{\Delta \tau_n}{\tau_n} \simeq -1.5 \frac{\Delta m_e}{m_e} + 6.5 \frac{\Delta Q_{np}}{Q_{np}}. \tag{4.10}$$

The linearized variation in T_f further depends on m_e and Q_{np}, while t_N is mostly affected by the deuterium nuclear binding energy B_D [63]. Ref. [62] analyzed the impact of independently varying $\{Q_{np}, \tau_n, B_D, m_e\}$. Their consequences on the final abundances are shown in figure 4.2b which yields the constraints from the ^{4}He data at 2σ [1]

$$\begin{aligned} -8.2 \times 10^{-2} \lesssim & \frac{\Delta \tau_n}{\tau_n} \lesssim 6 \times 10^{-2} \\ -4 \times 10^{-2} \lesssim & \frac{\Delta Q_{np}}{Q_{np}} \lesssim 2.7 \times 10^{-2} \\ -7.5 \times 10^{-2} \lesssim & \frac{\Delta B_d}{B_d} \lesssim 6.5 \times 10^{-2}. \end{aligned} \tag{4.11}$$

These bounds are valid for independent variations, meaning that the authors held τ_n fixed for individual variations in Q_{np} and m_e.

Variation from $m_n - m_p$

By definition, $m_n - m_p = Q_{np}$ and our estimate from section 3.3.2 for required variation to allow the TDS of $\Delta Q_{np}/Q_{np} \simeq 0.015$ satisfies these constraints. From 4.10, the induced variation in the neutron lifetime $\Delta\tau_n/\tau_n \simeq 0.1$ is slightly larger than the limits, but it could be counter-balanced by a deviation in m_e. We can also notice that neglecting T_f, 4.8 tells us that Q_{np} and τ_n act in opposite direction, so the constraints

could potentially reconcile for a variation in Q_{np} only.

Variation from m_e

There are no quoted bounds in 4.11 for a simple variation of m_e with other parameters fixed; its most important effect is through τ_n. We find that the needed $\Delta\tau_n/\tau_n \simeq -0.06$ is allowed and thus the TDS is viable through an independent variation of m_e.

Variation from $\alpha_{\rm em}$

The effect of the fine-structure constant on BBN is more subtle and complex. In addition to the 4 basics parameters, it also affects all reaction rates. The authors of ref. [64] argued that

$$-8.9 \times 10^{-2} < \frac{\Delta\alpha_{\rm em}}{\alpha_{\rm em}} < 1.6 \times 10^{-2}, \tag{4.12}$$

in agreement with ref. [65].

While these bounds do not forbid the TDS, we *cannot* consider the TDS solely with the variation of $\alpha_{\rm em}$ as many studies (see section 3.2.2) have shown it has a strong impact on the CMB physics. In this work, we do not consider any other effect than the TDS and thus a variation in the excess energy of tritium decays is not applicable to our analysis.

Timescale considerations

The T $\rightleftarrows$ ^{3}He interactions we are considering in the TDS arise from weak interactions. We saw that such interactions become inefficient under 1 MeV and BBN starts after the freeze out of proton-neutron freeze out. Therefore, any weak interaction T $\rightleftarrows$ ^{3}He is subdominant in BBN and can safely be neglected in the network of nuclear reactions (figure 4.1). For example, the SM decay T $\rightarrow$ ^{3}He has a lifetime of $\sim$12 years, which is much longer than the BBN timescale and is disregarded in BBN. Similarly, the reaction ^{3}He $\rightarrow$ T through electron capture allowed for negative Q in the TDS will not be efficient for free electrons. The accumulation of tritium will start after helium recombination, where the proximity of the orbiting electron enhances the reaction cross-section.

4.2 Ionization History

4.2.1 Recombination

Once the light nuclei have been created, the universe has to cool down to an eV-scale temperature, roughly 300 000 years later, to form electrically neutral atoms. At this point, it is a good approximation to consider only hydrogen and ^{4}He, since all other nuclei add up to less than 1 part in 10^{-4}. The relevant binding energies B for recombination are therefore

$$B_{^4\mathrm{He}^+} = 54.4 \text{ eV}, \qquad B_{^4\mathrm{He}} = 24.6 \text{ eV}, \qquad B_{\mathrm{H}} = 13.6 \text{ eV}. \tag{4.13}$$

Because of the hierarchy in binding energies, the full recombination process is divided into 3 stages, recombination of the doubly ionized then singly ionized ^{4}He, ending with hydrogen.

The Saha equation B.9 can be used for He

$$\frac{n_e n_{\mathrm{He}^{i+1}}}{n_{\mathrm{He}^i}} = \frac{n_e^{(0)} n_{\mathrm{He}^{i+1}}^{(0)}}{n_{\mathrm{He}^i}^{(0)}}, \tag{4.14}$$

where $i = \{0, 1\}$ represents the ionized number of He and photons have been taken at equilibrium $n_\gamma = n_\gamma^{(0)}$. The ionized fractions of helium are defined as $X_{\mathrm{He}^{++}} = n(\mathrm{He}^{++})/n_{\mathrm{He}}$ and $X_{\mathrm{He}^+} = n(\mathrm{He}^+)/n_{\mathrm{He}}$, where the denominator n_{He} is the total number of helium nuclei. Using the definition for the number densities n and $n^{(0)}$ (see B.5 and B.6), we can rewrite 4.14 as [66]

$$\frac{n_e X_{\mathrm{He}^{i+1}}}{X_{\mathrm{He}^i}} = \frac{2g_{i+1}}{g_i} \left(\frac{m_e k_B T_b}{2\pi\hbar^2} \right)^{\frac{3}{2}} \mathrm{e}^{\frac{-B_{\mathrm{He}^i}}{k_B T_b}}, \tag{4.15}$$

where $i = \{0, 1\}$, $X_{\mathrm{He}} = 1 - X_{\mathrm{He}^+} - X_{\mathrm{He}^{++}}$ and the degeneracy factors are $g_{0,1} = 1$, $g_2 = 2$.

For hydrogen, the high number of energetic photons emitted distorts the thermal spectrum of radiation and the system can no longer be taken at equilibrium. One therefore has to use the full Boltzmann equation B.8

$$a^{-3} \frac{\mathrm{d}(n_e a^3)}{\mathrm{d}t} = \langle \sigma v \rangle \left\{ n_H \frac{n_e^{(0)} n_p^{(0)}}{n_H^{(0)}} - n_e^2 \right\}. \tag{4.16}$$

When thermal equilibrium is reached, excited states are almost completely depleted

$$\frac{n_{2P}}{n_{1S}} = \frac{g_{2P}}{g_{1S}} \mathrm{e}^{-\frac{3}{4}\frac{B_H}{T}} < 10^{-10} \qquad \text{for } T < 5000 \text{ K}, \tag{4.17}$$

the neutralization of a particular atom is therefore only complete when it lies in the ground state. In calculating the cross section included in 4.16, we consider only cascading recombination, meaning that the hydrogen atom is produced in an excited state and then decays to the $1S$ ground state. A direct recombination to the ground state emits a 13.6 eV photon that ionizes another hydrogen, resulting in no net change. The Lyman-α transition $2P \to 1S$ also does not yield a significant increase in n_{1S} because the Lα photon excites another hydrogen atom to the $2P$ state. The most efficient reaction is through the $2S \to 1S$ transition, which is forbidden with 1 photon due to angular momentum conservation (see for eg. [67] and the selection rules). The decay is allowed in second order perturbation through the 2-photon decay at a much slower rate.

$$\Gamma_{2S\to 1S} \simeq 8.23 \text{ s}^{-1} \quad \ll \quad \Gamma_{2P\to 1S} \simeq 4 \times 10^8 \text{ s}^{-1} \tag{4.18}$$

Evaluating the equilibrium number densities with B.6 and defining the ionized hydrogen fraction $X_H \equiv \frac{n_e}{n_e + n_H}$, we get [66]

$$\frac{\mathrm{d}X_H}{\mathrm{d}t} = C_r \left\{ (1 - X_H)\beta - X_H^2 n_b \alpha^{(2)} \right\}, \tag{4.19}$$

where the baryon number density $n_b = n_p + n_H$ refers to the number hydrogen nuclei and

$$\beta = \alpha^{(2)} \left(\frac{m_e T_b}{2\pi} \right)^{\frac{3}{2}} \mathrm{e}^{\frac{-B_H}{T_b}} \qquad \alpha^{(2)} = \langle \sigma v \rangle \tag{4.20}$$

$$C_r = \frac{\Gamma_\alpha + \Gamma_{2S\to 1S}}{\Gamma_\alpha + \Gamma_{2S\to 1S} + \beta^{(2)}} \qquad \Gamma_\alpha = \frac{8\pi \dot{a}}{a \lambda_\alpha^3 n_{1S}} \tag{4.21}$$

$$\beta^{(2)} = \beta \mathrm{e}^{\frac{\nu_\alpha}{T_b}} \tag{4.22}$$

β corresponds to the ionization rate and $\alpha^{(2)}$ to the recombination rate through 2γ decays from the $2S$ state or when the Lα photon is redshifted out of the resonance line before it excites another hydrogen. C_r is a the correction factor accounting for the ionization of excited states before they decay.

While the universe becomes neutral, the Thomson scattering rate, keeping the

baryons[1] in thermal equilibrium with radiation, decreases rapidly and the matter temperature T_b separates from the photon temperature T_γ. Therefore, T_b has to be tracked independently with [68]

$$\frac{\mathrm{d}T_b}{\mathrm{d}t} = -2\frac{\dot{a}}{a}T_b - \frac{8\sigma_T a_R T_\gamma^4}{3m_e c}\frac{X_e}{1+f_{\mathrm{He}}+X_e}(T_b - T_\gamma), \tag{4.23}$$

where $a_R = \frac{\pi^2 k_B^4}{15c^3\hbar^3}$ is the radiation constant and σ_T the Thomson cross section.

This treatment of recombination is an effective three-level atom model pioneered by Peebles [69] in 1968. Nowadays, with modern computers, it is easy to solve multi-level recombination and incorporate a careful treatment with the photon bath. Seager *et al.* [68] found that these additional effects could be accounted for by simply adding a fudge factor and a correction function to the recombination rate of 4.19. Their code, RECFAST, numerically solves for the ionized fraction and temperature. The result using WMAP-7 best-fit parameters [22] is shown in figure 4.3. The plotted value is the total ionized fraction $X_e = X_H + f_{\mathrm{He}}X_{He}$ which exceeds 1 when He is ionized.

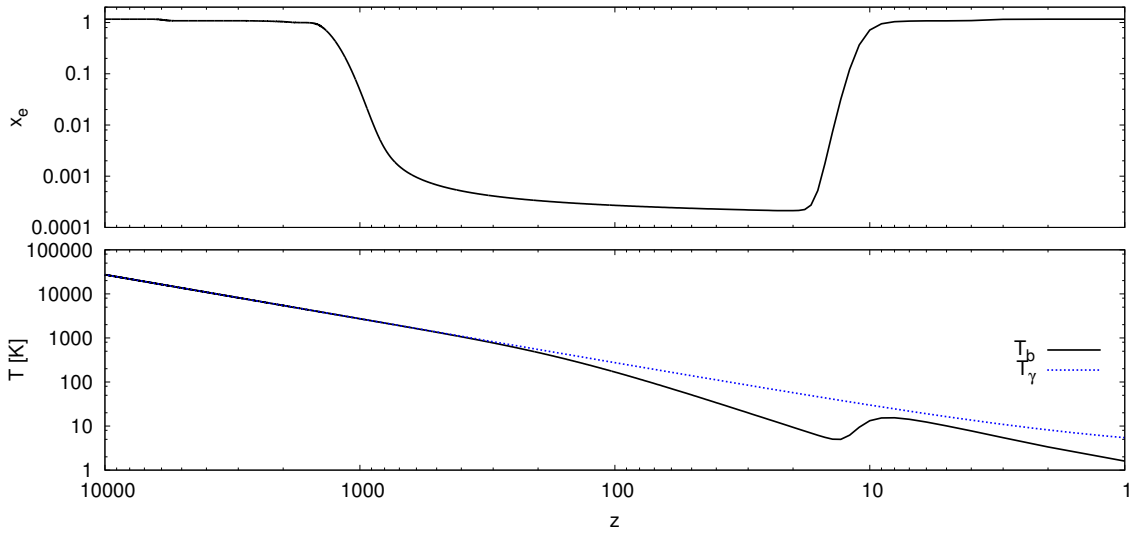

Figure 4.3: Ionized fraction and temperature as a function of redshift in the fiducial ΛCDM cosmology.

[1] In cosmology, baryons is a misnomer for matter, which includes the electrons, a lepton.

4.2.2 Reionization

Once the first galaxies form, the universe undergoes a complete reionization. There are multiple experimental observations justifying this phenomenon. For example, throughout the cosmic evolution, energetic photons are eventually redshifted to the L_α resonance corresponding to the transition between the ground and first excited states of neutral hydrogen. In a neutral universe, these photons should be absorbed and a "Gunn-Peterson trough" is observed in the photon spectra. However, these absorption lines are not as strong for low redshifts, suggesting an ionized cosmic medium [70]. Similarly, the detected [22] increasing in the large-angle polarization anisotropy of the CMB motivates the late-time reionization (see section 5.3.6). These evidences explain the increase of X_e at $z \simeq 10$ in figure 4.3.

4.3 Implementing delayed Tritium Decays by injecting energetic electrons

The tritium decays induced by varying constant (see section 3.4) can significantly alter the ionization history of the Universe. The effect of energy injection in the universe has already been investigated in the context of decaying or annihilating dark matter [71, 72, 73, 74, 75, 76, 77]. The scenario here is different in the sense that particles are not decaying from pre-recombination times with lifetimes long enough to add ionizing energy in the recombination process, but rather starts at some specific time, when $Q(t)$ becomes positive, with a time-varying decay rate.

The common technique in the literature to phenomenological analyze the injection of energy in the cosmic medium is through the *on-the-spot* approximation [73]. The effect is decomposed in two stages, where firstly the energetic particle is thermalized and then the extra energy is assumed to locally interact with the cosmic medium, instantaneously altering the thermal composition of the universe. The task is therefore to determine the cooling channels and accordingly examine how they influence the cosmic fluid.

4.3.1 Energy deposition of electrons

When non-relativistic electrons are inserted in the IGM, their kinetic energy is distributed to the gas through three types of interactions : collisional ionization of H,

He and He^+, collisional excitations of the same three elements and Coulomb collisions with thermal electrons [78]. Relativistic electrons are dominantly thermalized through inverse Compton scattering with the photons [73], but this process is negligible for the tritium decay scenario as the maximal average kinetic energy is ~ 6 keV (see section 3.4.1).

The distribution of energy between the seven channels is a statistical process weighted by the cross section of each interaction and the abundance of each particle. Monte Carlo simulations [79, 78, 80] have been done to estimate the fraction of energy deposited into ionizations, excitations and heat. The results found in ref. [78] are shown in figure 4.4. They used the assumptions that n(He)= 0.1n(H) and that H and He both have the same ionized fraction. Qualitatively, the fraction of energy that goes into heat should go to 1 has $x_e \to 1$ since there are no more neutral elements to ionize or excite. Consequently, they fit equations of the form

$$y = C[1 - (1 - x^a)^b] \qquad \text{or} \qquad y = C(1 - x^a)^b \tag{4.24}$$

depending on its behaviour at $x_e = 1$. The value of the fitting parameters of each curve in figure 4.4 are given in table 4.1. The analytic curves are only valid for $E_0 > 100$ eV and the error is the largest for the heating fraction at about $\sim 2\%$. For smaller primary energy, the curves have the same shapes, with the heat fraction being more dominant.

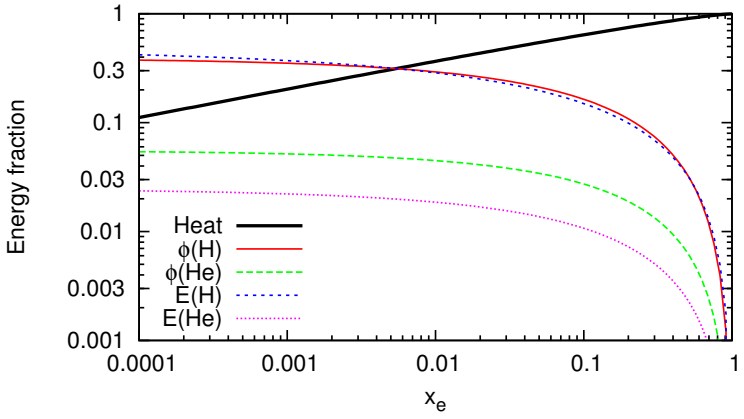

Figure 4.4: Energy fraction deposited in heat, ionization (ϕ) and excitation (E) of H and He as a function of the ionized fraction of the gas.

	C	a	b
Heat	0.9971	0.2663	1.3163
ϕ (H)	0.3908	0.4092	1.7592
ϕ (He)	0.0554	0.4614	1.6660
E (H)	0.4766	0.2735	1.5221
E (He)	0.0246	0.4049	1.6594

Table 4.1: Fitting parameters of the curves in figure 4.4 modeled as equation 4.24 to heat, ionization (ϕ) and excitation (E) energies.

4.3.2 Partial Reionization through Tritium Decays

To quantify the cosmological effect of the three cooling mechanisms, we adapt the prescription of ref. [72] to a time-varying decay rate. The modified ionization history is calculated by inserting new terms in the differential equations governing the ionized fraction of hydrogen, helium-4 and matter temperature (see 4.19 and 4.23). The number of particle of species i being ionized during by $|\mathrm{d}N|$ electrons injected in the cosmic medium is given by

$$\mathrm{d}n_i = \frac{\chi_i E_{avg}}{B_i}|\mathrm{d}N|, \tag{4.25}$$

where B_i is the ionizing energy (13.6 eV for hydrogen), E_{avg} the average kinetic energy of the electrons and χ_i the fraction of energy that is used to ionized this particular species (found in section 4.3.1). The number of injected electrons is found by generalizing the equation for decaying particle with a time-varying decay rate.

$$\mathrm{d}N = -\Gamma(t)N(0)\mathrm{e}^{-\int_0^t \Gamma(t')\mathrm{d}t'}dt \tag{4.26}$$

Dividing by the total number of number of hydrogen nuclei, we find the change in ionized fraction of species i as a function of redshift

$$\left.\frac{\mathrm{d}X_{[\mathrm{H,He}]}}{\mathrm{d}z}\right|_{\mathrm{TDS}} = \frac{-1}{H(z)(1+z)}\chi_i(z)\frac{E_{avg}(z)}{B_{[\mathrm{H,He}]}}\Gamma(z)\frac{Y_T}{A_{[\mathrm{H,He}]}}\mathrm{e}^{-\int_{t_0}^t \Gamma(t')\mathrm{d}t'}, \tag{4.27}$$

where the first fraction comes from the change of variable $\frac{\mathrm{d}t}{\mathrm{d}z}$, $Y_T = \frac{N_T(0)}{n_b}$ is the initial fractional amount of tritium, $A_{[\mathrm{H,He}]} = \{1, f_{\mathrm{He}}\}$ for {H, He} to correct for the proper denominator in the definition of X_{He} and t_0 the cosmic time at which the tritium decay starts.

We initially assume negative Q so that the ^{3}He fraction from BBN (see figure 4.2a) all decayed into tritium and take $Y_T = 10^{-5}$. More precisely, using the lifetime of ^{3}He

as a function of $\tilde{Q} = -Q$ from 3.21 and that there is $\sim 3 \times 10^5$ years between the full recombination of He and the CMB emission time, ^{3}He will be mostly depleted if we have

$$Q(\text{He recombination}) \lesssim -15 \text{ keV}. \tag{4.28}$$

Moreover, the fraction of energy that is dissipated through excitations increases the ionized fraction. Indeed, photoionization is more effective for excited electrons and thus yields the extra term [72, 81]

$$\left.\frac{\mathrm{d}X_H}{\mathrm{d}z}\right|_{\text{TDS},n=2} = \frac{-1}{H(1+z)}(1-C_r)\chi_\alpha(z)\frac{E_{avg}(z)}{E_2}\Gamma(z)Y_T \mathrm{e}^{-\int_{t_0}^{t}\Gamma(t')\mathrm{d}t'}, \tag{4.29}$$

where C_r is the correction factor from 4.21, χ_α the fraction of energy that goes into H excitations to $n = 2$ and $E_2 = 10.2$ eV the energy required per excitation. We assume that all excitations are to the first excited state and the $(1 - C_r)$ factor gives the probability an $n = 2$ electron is ionized before decaying to the ground state. The true scenario lies somewhere between this optimistic approximation and no treatment of these excitations as excitations can happen between different energy levels [76]. A more precise study would require a full radiative transfer calculation.

Since the universe is mostly comprised of monoatomic molecules, we know from classical thermodynamics that the kinetic energy of each particles is $E_{kin} = \frac{3}{2}k_B T$ [82]. Therefore, the change in matter temperature is given by

$$\frac{\mathrm{d}T_b}{\mathrm{d}z} = \frac{-1}{H(z)(1+z)}\frac{2}{3k_B}\frac{\chi_h(z)E_{avg}(z)}{1+X_e+f_{He}}\Gamma(z)Y_T \mathrm{e}^{-\int_{t_0}^{t}\Gamma(t')\mathrm{d}t'}, \tag{4.30}$$

where χ_h is the fraction of energy that goes into heat.

We insert these extra terms in the corresponding differential equations of RECFAST and solved for the modified histories, keeping z_0 and Δz from our $Q(z)$ ansatz 3.22 as free parameters. Three examples are shown in figure 4.5 for timescales shorter than the Standard Model half-life of tritium. The instantaneous extra ionization is maximized at $\Delta X_e \simeq 10^{-3}$ for all three, but the residual fraction is lower for larger z_0 since recombination is still efficient. For $z_0 \gtrsim 1000$, most energy goes into heat since the universe is already ionized. For large z_0, we also observe a spike in the temperature difference. This due to the strong coupling with radiation, any deviation from the radiation temperature is quickly drawn back from the $(T_b - T_\gamma)$ term in 4.23.

A variation of Q through a change in m_e will have higher order effects on the

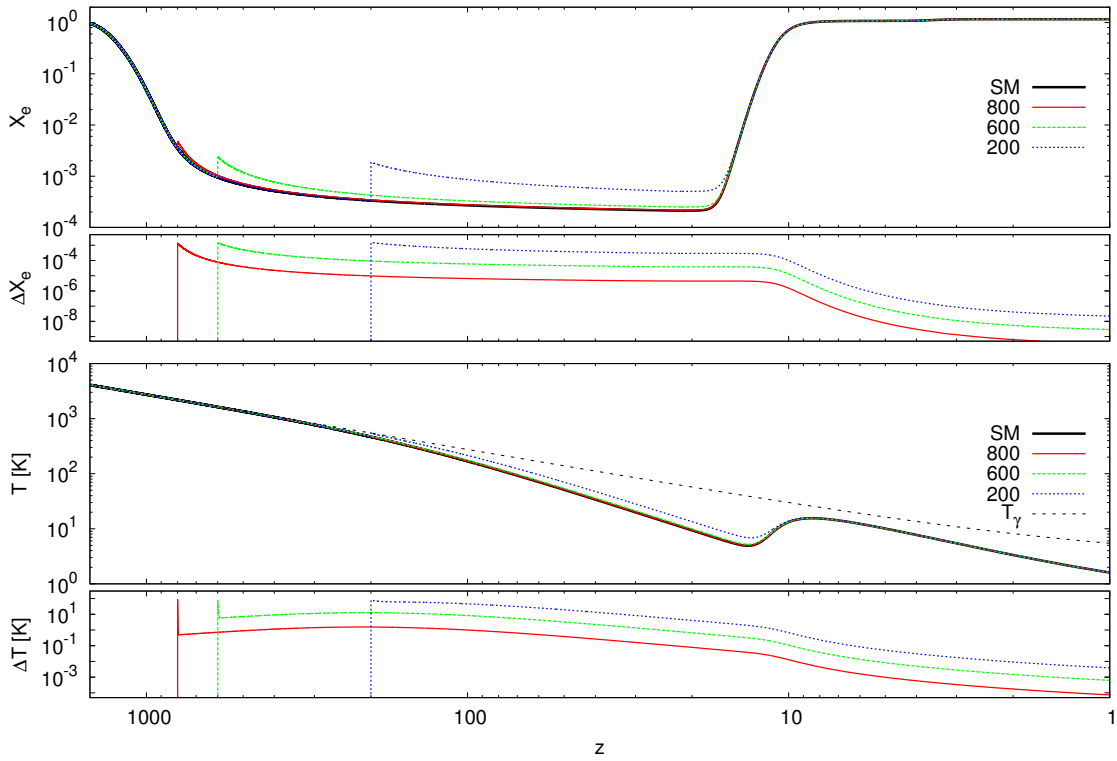

Figure 4.5: Ionized fraction and temperature as a function of redshift for T decays starting at $z_0 = 800$, 600 and 200 with $\Delta z = 10^{-4}$. The difference with the fiducial cosmology is also shown.

ionization history. In particular, the Thomson cross section

$$\sigma_T = \frac{8\pi}{3}\frac{\hbar^2}{m_e^2 c^2}\alpha_{\rm em}^2, \tag{4.31}$$

will be slightly modified for a Δm_e and should be considered for a more precise treatment.

4.4 Visibility of the Past

The photons we detect today contain information about the medium they last scattered with. Had the cosmic medium discontinuously changed from opaque to transparent, the photons would give us a perfect picture of the universe at that exact moment. However, the continuous decrease of the ionized fraction over a redshift range of $\Delta z \sim 300$ and the non-zero residual fraction mean that some photons re-

scatter through Thomson scattering between the present day and $z \simeq 1000$. The observed image is therefore an integrated story of the universe.

Quantitatively, the probability of a photon to scatter in an interval Δt is $\frac{\Delta t}{\tau_{\rm T}}$, where $\tau_{\rm T} = (\sigma_{\rm T} n_e)^{-1} = (\sigma_{\rm T} X_e n_t)^{-1}$ is the mean free time for Thomson scattering and is assumed to be constant during the time interval. Then, the probability a photon last scattered around time t and traveled freely to t_0 is [2]

$$P(t+\Delta t) = \frac{\Delta t}{\tau_{\rm T}(t)} \left(1 - \frac{\Delta t}{\tau_{\rm T}(t-\Delta t)}\right) \cdots \left(1 - \frac{\Delta t}{\tau_{\rm T}(t_0)}\right). \tag{4.32}$$

Taking the $\Delta t \to 0$ limit, we get the visibility function $g(z)$

$$g(z) = \frac{{\rm d}\kappa}{{\rm d}z} {\rm e}^{-\kappa(z)}, \tag{4.33}$$

where we defined the optical depth $\kappa(z)$

$$\kappa(z) = \int_0^z \frac{{\rm d}z'}{H \tau_{\rm T}(z')} \tag{4.34}$$

and H is the Hubble rate at z. The visibility function tells us the distribution of last scattering epochs of the CMB photons. In figure 4.6, it is shown for a standard cosmology and different values of the T decay scenario. We notice that the enhanced residual ionized fraction from T decay augments the visibility of the so-called dark ages, between $z \sim 800$ and reionization, while reducing the signal from the peak by $\sim 1\%$.

4.5 Matter temperature sensitivity

In the following chapters, we will discuss the detectability of the TDS in the CMB information. We will see that it depends on the visibility function and therefore the ionization history. The matter temperature T_b has only the indirect effect of influencing X_e through the differential equations.

Another cosmological probe, the 21 cm line between the hyperfine splitting of the hydrogen ground state is directly sensitive to the matter temperature [83]. The effects of energy injection from dark matter decays have already been studied [84, 85], which is analogous to the TDS. Qualitatively, the increased matter temperature in the TDS should damp the differential brightness temperature in the absorption region

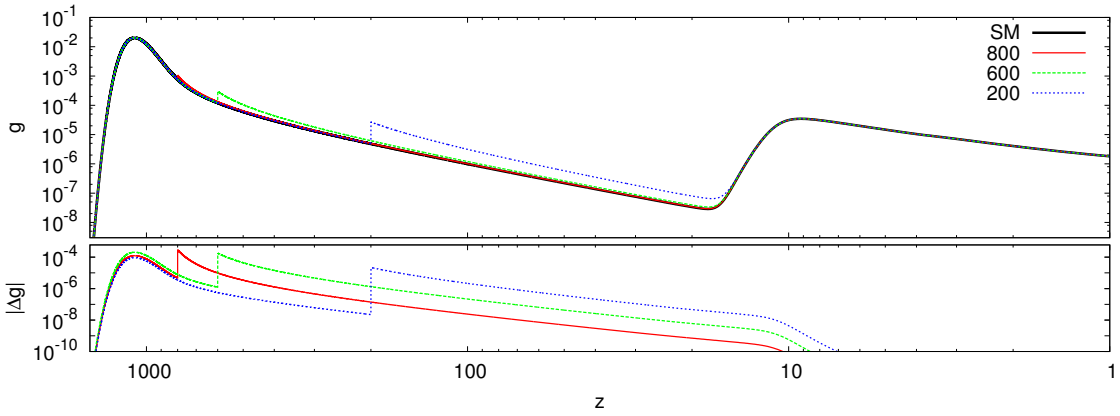

Figure 4.6: Visibility function as a function of redshift for T decays starting at $z_0 = 800$, 600 and 200 with $\Delta z = 10^{-4}$. The unsigned difference with the fiducial cosmology is also shown; before z_0, $g(z) < g_{SM}(z)$, and once the T decay is turned on, $g(z) > g_{SM}(z)$.

$30 \leq z \leq 300$ which could provide additional sensitivity to the scenario and complement the CMB constraints.

4.6 Energy injection in the photon bath

The blackbody photon distribution of the CMB photons has been measured very precisely by the COBE satellite [10]. Energy injection in the Universe can potentially alter the photon distribution and is constrained by the data. In the TDS, the maximal energy is released for small Δz. In this case, we can estimate the deposited energy per photon as

$$E_{TDS/\gamma} = K_e(Q_{SM})\frac{n_T}{n_\gamma} = K_e(Q_{SM})Y_T\eta_B \sim 10 \text{ keV } 10^{-5}10^{-10} \tag{4.35}$$

$$\sim 10^{-12} \text{ eV per photon,} \tag{4.36}$$

which is very small and show not impact the radiation spectrum.

Chapter 5

Cosmic Microwave Background

The Cosmic Microwave Background (CMB) is the earliest luminous signal detectable. It gives us a (blurred[1]) snapshot of the universe when it became transparent, around 300000 years after the Big Bang. It contains information about the constituents and primordial fluctuations that ultimately evolved into our present universe.

We briefly review the theoretical framework of the CMB and how we can extract useful information about the early state of the universe. We then discuss the implications of the tritium decay scenario on this primitive light.

5.1 Perturbations in the Universe

The small deviations in the CMB temperature shown in figure 1.1 (of order 10^{-5} with respect to base temperature [86]) suggest the perturbations sourcing these deviations are tiny. For this reason, we can properly follow their evolution to linear order. Any quadratic term will thus be very small and can be safely neglected.

The inhomogeneities in the universe force the metric to deviate from a smooth background. The metric perturbations are influenced by all types of particles, while the electrons interact with photons and protons through Compton and Coulomb scattering. To determine the present distribution of photons, we therefore need to solve simultaneously for all components, accounting for their couplings between each other. We here discuss the origin and general features of the perturbations. (See for eg. [66] for the full set of equations.)

[1]The image is weighted over time by the visibility function shown in figure 4.6.

5.1.1 Metric Perturbations

The information on the curvature of spacetime in entirely encoded in the rank-2 tensor metric $g_{\mu\nu}$. One can add three types of perturbations, namely scalar, vector or tensor perturbations. The SVT Decomposition Theorem [58] tells us that they decouple and evolve independently. For simplicity, we only consider scalar perturbations. Vector deviations are always irrelevant as they quickly decay with expansion [87] and the ratio of tensor to scalar perturbations is bounded to $r < 0.36$ by present observations [3]. The main contribution thus comes from scalar perturbations.

In the conformal longitudinal gauge, the smooth Robertson-Walker metric (equation 2.7) with flat geometry ($\kappa = 0$) is modified to [66]

$$ds^2 = a^2(\eta)\left\{-(1+2\psi)d\eta^2 + (1-2\phi)dx^i dx^i\right\}, \tag{5.1}$$

where the perturbations are parametrized by two scalar potentials $\psi, \phi \ll 1$ and η is the conformal time. There are other possible choices of gauge such as the commonly used synchronous gauge. Ultimately they yield the same physics, so the choice is a matter of preference and simplicity. The advantages of the longitudinal gauge are that the metric is diagonal, thus simplify the algebra, and the scalar perturbations are directly related to the gauge-invariant Bardeen potentials [88] ($\phi = -\Phi_H$, $\psi = \Phi_A$).

These scalar potentials are sourced by changes in the energy density filling spacetime. Their evolution can be tracked by solving the linearly perturbed version of Einstein equations 2.1.

5.1.2 Particle Distribution Fluctuations

In conjunction with the metric perturbations, each type of particles have a slightly modified phase-space distribution. The evolution is guided by the unintegrated Boltzmann equation

$$\frac{\mathrm{d}f}{\mathrm{d}t} = \frac{\partial f}{\partial t} + \frac{\mathrm{d}x^i}{\mathrm{d}t}\frac{\partial f}{\partial x^i} + \frac{\mathrm{d}p}{\mathrm{d}t}\frac{\partial f}{\partial p} + \frac{\mathrm{d}\hat{p}^i}{\mathrm{d}t}\frac{\partial f}{\partial \hat{p}^i} = C[f], \tag{5.2}$$

including the relevant collision terms $C[f]$ for the interacting species. The unperturbed phase-space distribution f_0 only depends on the total momentum $p = |\vec{p}|$ of the particles whereas perturbations can spoil homogeneity and isotropy. We can therefore expand the distribution f with new variables quantifying the perturbations

in each species.

Non-relativistic particles

Dark matter perturbations have to be treated in a specific way since their statistical distribution f_0 is unknown. We can observe their total number density and velocity, which are related to the phase-space distribution with

$$n_{\rm dm} = \int \frac{{\rm d}^3 p}{(2\pi)^3} f_{\rm dm} \tag{5.3}$$

$$v^i = \frac{1}{n_{\rm dm}} \int \frac{{\rm d}^3 p}{(2\pi)^3} f_{\rm dm} \frac{p\hat{p}^i}{E}. \tag{5.4}$$

We therefore define the dark matter perturbation δ as [66]

$$n_{\rm dm} = n_{\rm dm}^{(0)} \left[1 + \delta(\vec{x}, t)\right] \tag{5.5}$$

and integrate 5.2 in Fourier space to find

$$\dot{\delta} + ikv = -3\dot{\phi}, \tag{5.6}$$

where the overdot represent the derivative with respect to the conformal time ($\dot{} \equiv \frac{\partial}{\partial \eta}$). The velocity term v is a first order perturbation since it has a directional dependence. Integrating 5.2 with respect to the first moment in p instead yields

$$\dot{v} + \frac{\dot{a}}{a} v = -ik\psi. \tag{5.7}$$

In general, the $n^{\rm th}$ integrated moment of the Boltzmann equation will always depend on the $(n+1)^{\rm th}$ moment. However, since dark matter is *cold*, high moments are negligible at linear order and all the dark matter distribution is fully determined by δ and v [59].

Similarly, since baryons are also non-relativistic, their higher moments are irrelevant and their evolution can be parametrized by δ_b and v_b. Their evolution equations are similar to dark matters ones, with the addition of the Coulomb interaction term.

Relativistic Particles

For Standard Model particles which we know the statistics (the form of f_0), we can explicitly evaluate 5.2 and get the full information to follow the distribution during the cosmic evolution. For example, we can write for photons

$$f(\vec{x}, p, \hat{p}, t) = \left[\exp\left\{\frac{p}{T(t)[1+\Theta(\vec{x},\hat{p},t)]}\right\} - 1\right]^{-1}, \tag{5.8}$$

since it is a boson. We have identified the perturbation in the photon bath temperature $\Theta = \frac{\delta T}{T}$ in a specific direction $\hat{p}$ around the mean temperature T. Including the Compton interaction with the electrons, equation 5.2 for photons reduces to linear order to [89]

$$\dot{\Theta} + ik\mu\Theta = \dot{\phi} - ik\mu\psi + \dot{\kappa}\left(-\Theta + \Theta_0 + i\mu v_b + \frac{1}{2}\mathcal{P}_2(\mu)\Pi\right), \tag{5.9}$$

$$\Pi = \Theta_2 + \Theta_{P2} + \Theta_{P0}, \tag{5.10}$$

where we have switch again to Fourier k-space and κ is the optical depth defined in 4.34. We also defined the temperature monopole Θ_0 and quadrupole Θ_2 through the l^{th} multipole moment definition

$$\Theta_l \equiv \frac{1}{(-i)^l}\int_{-1}^{1}\frac{d\mu}{2}\mathcal{P}_l(\mu)\Theta(\mu), \tag{5.11}$$

with the Legendre polynomial $\mathcal{P}_l$ and $\mu \equiv \frac{\vec{k}\cdot\hat{p}}{k}$, the cosine angle between the wavenumber $\vec{k}$ and photon direction $\hat{p}$. Finally, the Compton amplitude involved in $C[f]$ has a polarization dependence, thus inducing polarization perturbations Θ_P to the photon spectrum through scatterings with electrons [90]. The Boltzmann evolution equation for polarization is given by [89]

$$\dot{\Theta}_P + ik\mu\Theta_P = \dot{\kappa}\left(-\Theta_P + \frac{1}{2}\left(1 - \mathcal{P}_2(\mu)\right)\Pi\right). \tag{5.12}$$

Massless neutrinos can be treated in the same way, neglecting the interaction in the parenthesis of 5.9.

5.1.3 Initial Conditions

The formulas for the perturbation variables in the distribution of dark matter, photons, baryons and neutrinos, together with the metric perturbations form a complete set of coupled differential equations that can be evolved in time. It might seem that there is freedom to choose initial conditions for each variable, thus allowing much arbitrariness in the large number of input parameters. However, in the early-time limit, where terms like the optical depth $\dot{\kappa}$ are vanishingly small, all variables can conveniently be related to ψ [59]. Therefore, the only choice in initial conditions lies in the ψ spectrum and fixes the evolution of all other perturbations.

5.2 Power Spectra

The generation of fluctuations is a stochastic process, of which we only have one realization, our universe. The exact value of a variable X cannot be predicted and we have to resort to expectation values. Since we are considering random variations around the mean value, the expectation value vanishes $\langle X \rangle = 0$. However, we can extract the spread in variations through the variance and define the power spectrum P_X of the scalar variable X

$$\left\langle X(\vec{k}, t_0) X^*(\vec{k'}, t_0) \right\rangle = (2\pi)^3 \delta(\vec{k} - \vec{k'}) P_X(k). \tag{5.13}$$

The brackets $\langle \cdot \rangle$ represent a statistical and ensemble average over the distribution of random initial conditions. Statistical isotropy and homogeneity imply that different wavevector $\vec{k}$ are uncorrelated and P_X only depends on $k = |\vec{k}|$.

5.2.1 Initial Spectrum

We eventually want to compute the power spectra of different cosmological scenario and compare them to observations. The definition 5.13 includes an average over initial conditions allowed by a given model. The primordial perturbations come from quantum fluctuations enhanced to macroscopic scales by inflation. The simplest versions of inflation, with a single-field slow-roll scalar inflaton, predict a nearly scale-invariant spectrum [58]. The fluctuations are gaussian, adiabatic and we assume a primordial

spectrum for curvature perturbations ψ of the form

$$\left\langle \psi(\vec{k})\psi^*(\vec{k'}) \right\rangle = (2\pi)^3 P_\psi(k)\delta(\vec{k}-\vec{k'}) = (2\pi)^3 \frac{A_S k^{n_s-1}}{k^3}\delta(\vec{k}-\vec{k'}), \tag{5.14}$$

where we have defined the spectral index n_s and the amplitude A_S of scalar metric perturbations. A scale-invariant spectrum implies $n_s = 1$. Currently, the 7-year WMAP data suggests $n_s = 0.963 \pm 0.014$ with $A_s = 2.42 \times 10^{-9}$ normalized at $k = 0.002$ Mpc^{-1} [22].

5.2.2 Decomposition of temperature fluctuations

The photons we receive on Earth come from all directions, hence their temperature is a function defined on S^2. It therefore makes sense to decompose the anisotropy into spherical harmonics

$$\frac{\Delta T}{T}(\vec{x_0}, \vec{n}, t_0) = \sum_{l,m} a_{lm}(\vec{x_0}) Y_{lm}(\vec{n}). \tag{5.15}$$

The vector $\vec{x_0}$ corresponds to our vantage point of view and can be removed by a simple redefinition of the monopole term a_{00}. The dipole terms a_{1m} are affected by our local peculiar velocity around the solar system and the centre of galaxy, its information is thus not instructive on cosmological parameters. The temperature angular power spectrum C_l is defined as

$$\langle a_{lm} a^*_{lm} \rangle = \delta_{ll'}\delta_{mm'} C_l. \tag{5.16}$$

In a homogeneous and isotropic universe, the axis from which we define the spherical coordinates is irrelevant, and thus C_l's are independent of m.

With these definitions, we can use the orthogonality of the Y_{lm} to evaluate the variance of temperature fluctuations

$$\left\langle \frac{\Delta T}{T}(\vec{n}) \frac{\Delta T}{T}(\vec{n'}) \right\rangle = \frac{1}{4\pi} \sum_l (2l+1) C_l P_l(\mu), \tag{5.17}$$

where $\mu = \vec{n} \cdot \vec{n}'$. The temperature anisotropies are therefore completely parametrized by the C_l coefficients.

5.2.3 Theoretical Prediction of the C_l's

To relate the observations with our theoretical framework, we need to evaluate $\frac{\Delta T}{T} = \Theta$ at the present time for each multipole Θ_l, which can then be related to the power spectrum C_l. If we integrate 5.9 for each multipole moment, we get an infinite hierarchy of coupled equations since each l^{th} moment depends on the $(l+1)^{\text{th}}$. We saw for dark matter that the quadrupole and higher moments can be disregarded because it is cold; photons are however relativistic and we cannot afford neglecting them. Instead, we can formally integrate 5.9 over the past light-cone and get a computationally tractable solution of the form [89]

$$\Theta(k) = \int_0^{\tau_0} d\tau \mathrm{e}^{ik\mu(\tau-\tau_0)} S_T(k,\tau) \tag{5.18}$$

$$\begin{aligned} S_T(k,\tau) = g\left(\Theta_0 + \psi - \frac{\dot{v_b}}{k} - \frac{\Pi}{4} - \frac{3\ddot{\Pi}}{4k^2}\right) \\ + \mathrm{e}^{-\kappa}(\dot{\phi}+\dot{\psi}) - \dot{g}\left(\frac{v_b}{k} + \frac{3\dot{\Pi}}{4k^2}\right) - \frac{3\ddot{g}\Pi}{4k^2}. \end{aligned} \tag{5.19}$$

Then, the temperature source term S_T depends on the perturbation variables, the optical depth κ and visibility function g introduced in 4.33. The monopole Θ_0 and quadrupole Θ_2 can be evaluated to arbitrary precision with an appropriate truncation scheme in the hierarchy.

The geometric dependence is solely incorporated in the exponential multiplying the source function and the temperature anisotropy moments can be written as

$$\Theta_l(k,\tau_0) = \int_0^{\tau_0} S_T(k,\tau) j_l[k(\tau_0-\tau)] d\tau, \tag{5.20}$$

where j_l is the Bessel function of order l. Thus, we can evaluate the expectation value of the variance of the temperature fluctuations to find the theoretical prediction of the C_l's

$$C_l = \frac{2}{\pi} \int dk\ k^2 P_\psi(k) \Theta_l^2(k,\tau), \tag{5.21}$$

where P_ψ is the primordial spectrum.

5.2.4 Polarization correlations

We previously stated without justification through equation 5.12 that the complete Boltzmann evolution equation for the temperature perturbation Θ requires the simultaneous evolution of some polarization fluctuation Θ_P. At first sight, it might feel unnatural to incorporate such a term. After all, the high degree of isotropy and homogeneity of the Universe before recombination should produce an unpolarized photon bath. Its significance was first realized in 1968 by Rees [91].

Unlike the temperature perturbations, the polarization fluctuations are second order with respect to the primordial metric fluctuations. More precisely, partial polarization arises from Thomson scattering between radiation and a free electron. An unpolarized radiation plane wave becomes linearly polarized at a $\cos^2\theta$ percentage, when the angle between the incoming and outgoing radiation wave vector is θ [92]. Therefore, right-angle scattering produces fully polarized light. In an isotropic Universe, the symmetry of the photon bath cancels the local production of polarization. However, a net polarization is generated in an anisotropic Universe with a quadrupole moment in the temperature distribution [59].

Due to its oscillatory vector nature, linear polarization is a spin-2 object and some special care is needed for a correct expansion in spherical harmonics (see for eg. [92]). One can use spin-weighted [93] or tensor [94] spherical harmonics to expand the Stokes parameters representing the polarization. They can then be conveniently expressed in scalar representation through parity-invariant E-type or the pseudo-scalar B-type polarization, an obvious analogy to the classical electric and magnetic field as they respectively share the same curl and gradient-free properties.

In this thesis, we only consider E-mode polarization. Gradient-free B-mode polarization has not been observed yet due to its weak signal. Scalar metric perturbation only produce E-mode polarization and consequently an observable correlation in B-mode polarization would dominantly arise from tensor perturbation (gravity waves) [95]. In fact, looking for B-mode polarization is the primary means for a tensor perturbation detection and would provide deep information on the potential sourcing inflation [95], although some E-mode is transformed into B-mode through gravitational lensing [96].

The source term representing the E-mode polarization is [89]

$$S_E^l(k,\tau) = \frac{3}{4}\frac{g\Pi}{k^2(\tau_0-\tau)^2}\sqrt{\frac{(l+2)!}{(l-2)!}}, \tag{5.22}$$

where the square root term is needed for proper normalization of the tensor harmonics. We can therefore generalize the temperature correlation power spectrum in equation 5.21 to

$$C_l^{XY} = \frac{2}{\pi} \int dk\ k^2 P_\psi(k) \Theta_l^X \Theta_l^Y, \tag{5.23}$$

$$\Theta_l^X(k, \tau_0) = \int_0^{\tau_0} S_X(k, \tau) j_l[k(\tau_0 - \tau)] d\tau, \tag{5.24}$$

where X, Y can be temperature T, E or B mode polarization. Cross correlations such as C_l^{TE} are allowed and provide other observables with valuable information. To lighten the nomenclature, we will only write $C_l^X \equiv C_l^{XX}$, when we are not referring to cross correlations.

5.3 Anisotropies in the Sky

The temperature power spectrum has been observed with increasing precision in the past decade. In figure 5.1, we show the results from the 7-year data set of the WMAP satellite. The red curve corresponds to the theoretical predictions from 5.21 with best-fit parameters.

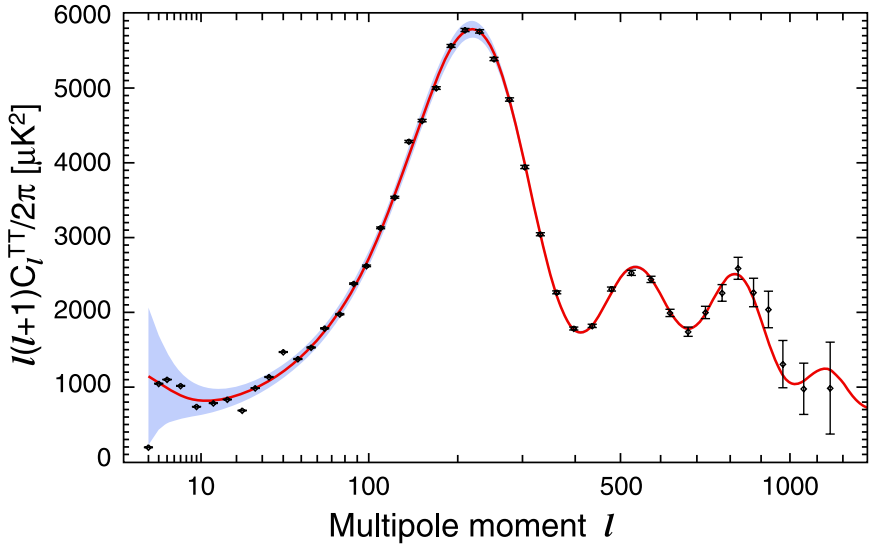

Figure 5.1: Temperature anisotropy from 7-year WMAP with cosmic variance in blue. Credit NASA/WMAP Science Team.

Although there are a few marginal data points at low l values, the agreement is

quite spectacular, confirming our understanding of cosmological perturbations. Here we review the physics behind the general features of the curve.

5.3.1 Cosmic Variance

Before we discuss the shape of the anisotropy spectrum, it is important to mention a word on the uncertainty of the measurements. Returning to our definition of the temperature inhomogeneity power spectrum C_l in 5.17, we can write it as

$$C_l^T = \frac{1}{4\pi} \int d^2\hat{n}\; d^2\hat{n}'\; P_l(\mu) \left\langle \frac{\Delta T}{T}(\hat{n}) \frac{\Delta T}{T}(\hat{n}') \right\rangle, \tag{5.25}$$

where we explicitly wrote the integration over all directions. However, experimentally we are fixed at one vantage point and cannot average over positions. What we actually observe is one realization of the expectation value [97]

$$C_l^{\text{obs}} = \frac{1}{4\pi} \int d^2\hat{n}\; d^2\hat{n}'\; P_l(\mu) \frac{\Delta T}{T}(\hat{n}) \frac{\Delta T}{T}(\hat{n}'). \tag{5.26}$$

The difference is known as the cosmic variance and is an intrinsic uncertainty that cannot be escaped in any CMB experiment. For each l, we can however average over m and larger l have more m measurements, thus reducing our uncertainty. Quantitatively, the cosmic variance is given by

$$\frac{\Delta C_l}{C_l} = \sqrt{\left\langle \left(\frac{C_l - C_l^{\text{obs}}}{C_l} \right)^2 \right\rangle} = \sqrt{\frac{2}{2l+1}} \tag{5.27}$$

and is shown is shaded blue in figure 5.1.

5.3.2 Large Scale

The large scale structure of the CMB is formed by perturbation wavevectors larger that the horizon at recombination. The horizon size at recombination is about $\theta \sim 1$ of separation in the sky, or equivalently $l \sim 200$ in spherical moments. By large scale, we therefore mean that we are looking at the behaviour of the small angular moments $l \ll 200$.

These fluctuations were not in causal contact at recombination and therefore did not evolve much since inflation. It is the clearest information we have on inflation

and is mostly influenced by P_ψ rather than the evolution terms $\Theta(k,\tau)$. Our choice of nearly flat primordial spectrum $P_\psi = A_S k^{n-1}$ predicts an almost flat plateau proportional to $l(l+1)$ with the slope determined by the spectral index.

Information on the large scale or small angular moment is difficult to extract as its significance is greatly reduced by the poor statistics inherent from the cosmic variance.

5.3.3 Acoustic Peaks

The most obvious feature in the C_l's is the oscillatory shape of the curve. Physically, the peaks arise from the oscillation between overdensed and underdensed states in the baryon-photon fluid, sourced by gravitational collapse and pressure.

Metric perturbations ψ are generated during the inflationary phase. The wavelength of each fluctuation Fourier mode eventually becomes larger that the Hubble radius H^{-1} and ψ stops evolving as it corresponds to acausal distances. Then, at horizon re-entry ψ sources density fluctuations δ which is affected by gravity and pressure [58]

$$\ddot{\delta} - c_s^2 \nabla^2 \delta = F_g[\psi], \tag{5.28}$$

where c_s speed of sound and F_g gravitational source term. If we approximate recombination to be instantaneous, then we observe in the CMB the phase of the oscillation 5.28 at recombination. Since the wavelengths re-enter the horizon at different times, we observe a coherent addition of all wavelengths, resulting in the peaks and troughs shown in figure 5.1.

5.3.4 Small Scale

The small scale anisotropy are represented by the large l behaviour of the power spectrum. The dominant Fourier modes have entered the horizon much before recombination and consequently had time to evolve.

The damping observed in the acoustic peaks arises from the photon collisions before decoupling. The interactions partially thermalize the plasma, which results in a diffusion damping, or Silk damping, of the small scale anisotropies [98]. If we consider the noninstanteneous recombination, there are extra collisions with the remaining free electrons, which increases the damping scale.

The photons carry information about their last scattering position, and we effec-

tively observe a weighted average over a scale $\Delta\eta_r$, the effective duration of recombination (or width of the visibility function, see figure 4.6). Then, inhomogeneities with scales smaller than $\Delta\eta_r$ are suppressed, resulting in an additional damping on the tail of the C_l's [2].

5.3.5 Polarization signal

The E-mode polarization anisotropy was first observed [99] by the DASI telescope in 2002. In the following years, multiple experiments aimed at measured the polarization multipole moments and their results are shown in figure 5.2.

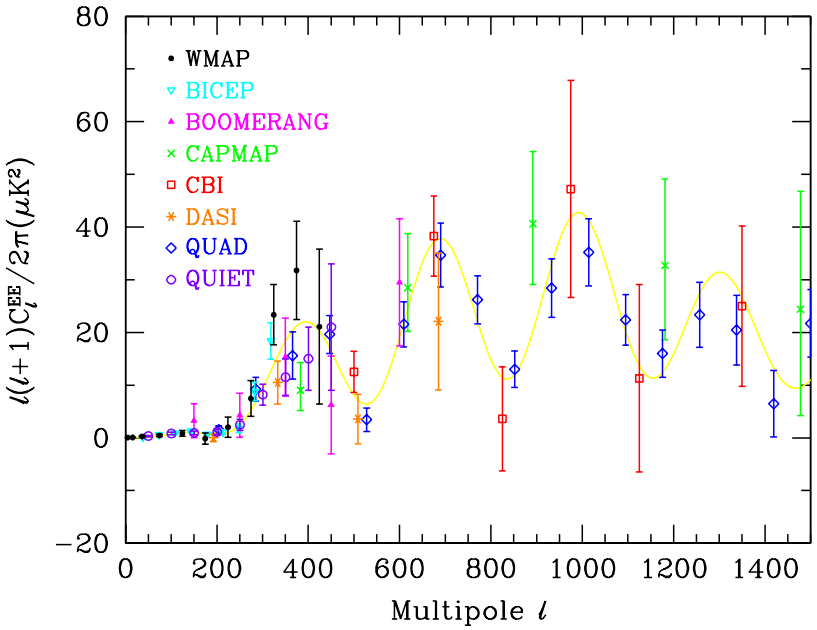

Figure 5.2: E-mode polarization anisotropy measurements from different experiments. Taken from [3].

Polarization gives us a cleaner view of the last scattering surface than the temperature signal. This is simply because the polarization of a photon does not change while free streaming, as opposed to its energy which is affected by the time-variation of the potentials and other effects. This is easily seen in the source functions, where S_E (5.22) is proportional to the visibility function and S_T (5.19) has extra terms. With their information put together, we are able to disentangle last scattering effects to other cosmological evolution ingredients, thus breaking degeneracies between parameters that were hard to extract with temperature alone.

5.3.6 Full reionization at low redshifts

As mentioned in section 4.2.2, the lack of Gunn-Peterson troughs in the Lyman-α spectrum suggests a completely ionized IGM at $z \sim 6$. Independently, the CMB polarization confirms the late reionization of the Universe although present data suggest a redshift of 10.5 [22].

Additional scatterings at low redshifts wash out the temperature correlations within the angular scale in the sky of the light-cone at the interaction time. Mathematically, this means that the observed power spectrum will be [2]

$$C_l^{T-\mathrm{obs}} = \begin{cases} C_l^T & l \ll l_{\mathrm{reio}}, \\ \mathrm{e}^{-\mu_{\mathrm{reio}}} C_l^T & l \gg l_{\mathrm{reio}}, \end{cases} \tag{5.29}$$

where μ_{reio} is the optical depth due to reionization only and C_l^T is the signal without reionization. For standard reionization, this damping is in almost perfect degeneracy with A_S, the amplitude of the scalar metric perturbation. Since the angular scale of a reionization at $z \sim 10$ corresponds to $l_{\mathrm{reio}} \sim 10$, the data in the range $l < l_{\mathrm{reio}}$ is dominated by cosmic variance and the two effects cannot be discriminated.

As previously mentioned, the polarization signal relates directly to the last scattering of the photons and gives a better picture of the ionization history through the visibility function. The increased ionized fraction at late times augments the Thomson collisions which induces polarization. Therefore, an extra peak centered at l_{reio} should be observed in the polarization power spectra, with an amplitude proportional to the fraction of rescattered photons $1 - \mathrm{e}^{-\mu_{reio}}$ and the temperature quadrupole at that redshift [2]. In figure 5.3, we show the temperature-polarization cross-correlation from WMAP that clearly corroborates the low redshift reionization.

5.4 Tritium Decay Scenario Effects

With a good understanding of the physics of the ΛCDM cosmic microwave background, we can look at the implications of the TDS and understand the correlation spectra differences with the standard cosmological scenario.

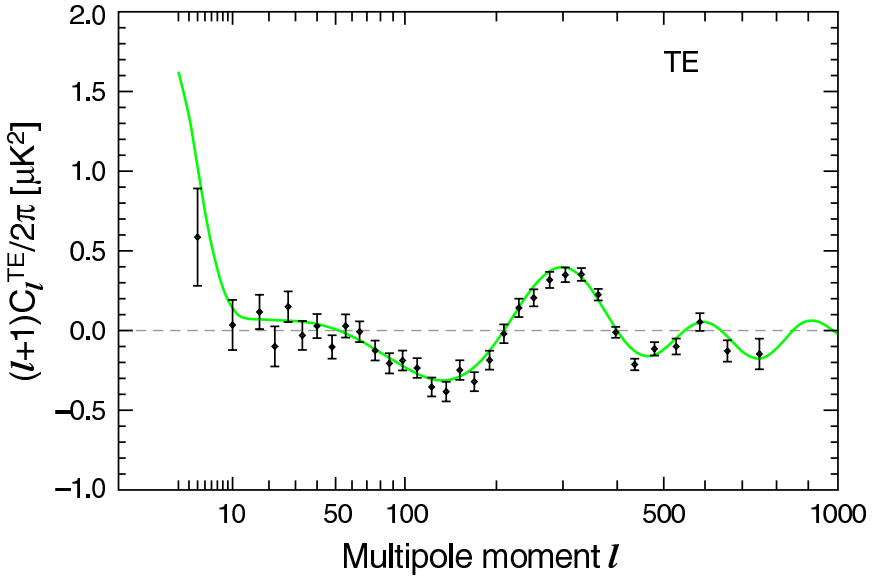

Figure 5.3: Temperature polarization cross-correlation measurements from WMAP 7-year data. Credit NASA/WMAP Science Team.

5.4.1 Temperature spectrum

The thermal physics of the TDS is comparable to the late-time reionization from the first generation of stars, with a different redshift and final ionized fraction. We can therefore expect the TT spectrum to be modified in a similar way to equation 5.29, with the characteristic angular moment approximated by

$$l_{TDS} \simeq \frac{\pi}{\Delta\theta_{TDS}} \simeq \pi\Omega_m^{0.09}\sqrt{z_{TDS}}, \tag{5.30}$$

where was have used a fitting formula from [2] for $\Delta\theta$.

To quickly scan this effect through the entire z_{TDS}-Δz space, we calculated the optical depth μ_{TDS} due to the TDS partial reionization and show the damping factor $e^{-\mu_{TDS}}$ in figure 5.4. As expected, short timescales in Δz yield greater damping, maximized for all $\Delta z \lesssim 10^{-3}$, which corresponds to timescales shorter than the SM lifetime of tritium. The damping reaches its largest value of $\sim 3\%$ around $z_{TDS} \sim 600$. For early z_{TDS}, recombination is still efficient and diminishes the freeze-out ionized fraction, thus reducing the C_l^{TT} damping factor. For small z_{TDS}, the residual ionized fraction is maximal, but it is integrated over a smaller redshift range and therefore results a reduced damping.

The theoretical CMB anisotropy power spectra can be obtained through equa-

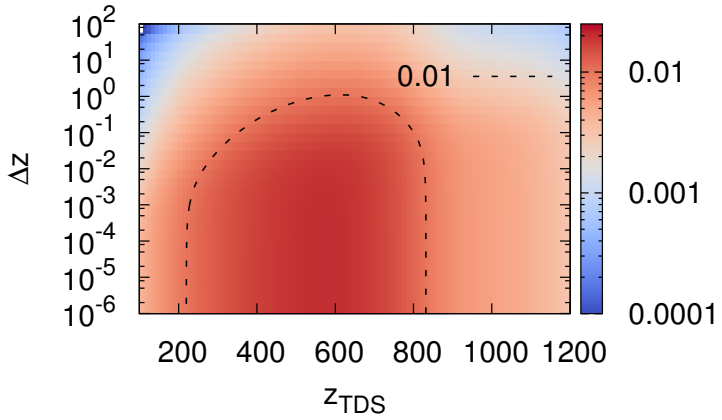

Figure 5.4: Damping factor of the high l tail of the C_l^T arising from the TDS. A dotted line corresponding to a factor of 1% is shown to guide the eye.

tion 5.21 by numerically integrating the large system of evolution equations. A variety of publicly available computer programs are designed to efficiently find the C_l's for any reasonable input parameters. We modified the most recent one on the market, CLASS [100] (the Cosmic Linear Anisotropy System Solver), to incorporate the TDS. In figure 5.5, we show C_l^T for 4 different redshift with $\Delta z = 10^{-4}$. The high-l tail behaviour is exactly as expected, with a damping of $1 - 3\%$.

An oscillatory feature appears for large z_{TDS}. This slight shift of the peak positions is a signature of a modified recombination redshift. Partial reionization appears near the maximum of the visibility function which is broadened towards lower redshifts (see figure 4.6). This effectively changes the angular scale of recombination and displaces the position of the acoustic peaks in the spectrum.

5.4.2 Polarization spectrum

Following our intuition from the full reionization from the first galaxies, we expect a rise in the polarization correlations on the large scale. In particular, the increase should start around our derived characteristic angular moment l_{TDS} and plateau for $l < l_{TDS}$. Moreover, the signal for earlier times is still partially washed out by the extra Coulomb collisions and the tail should behave with the same damping as in the temperature spectrum.

To better observe the effect of the TDS partial reionization, we show in figure 5.6 the EE polarization spectrum, for a universe with the ΛCDM parameters without the

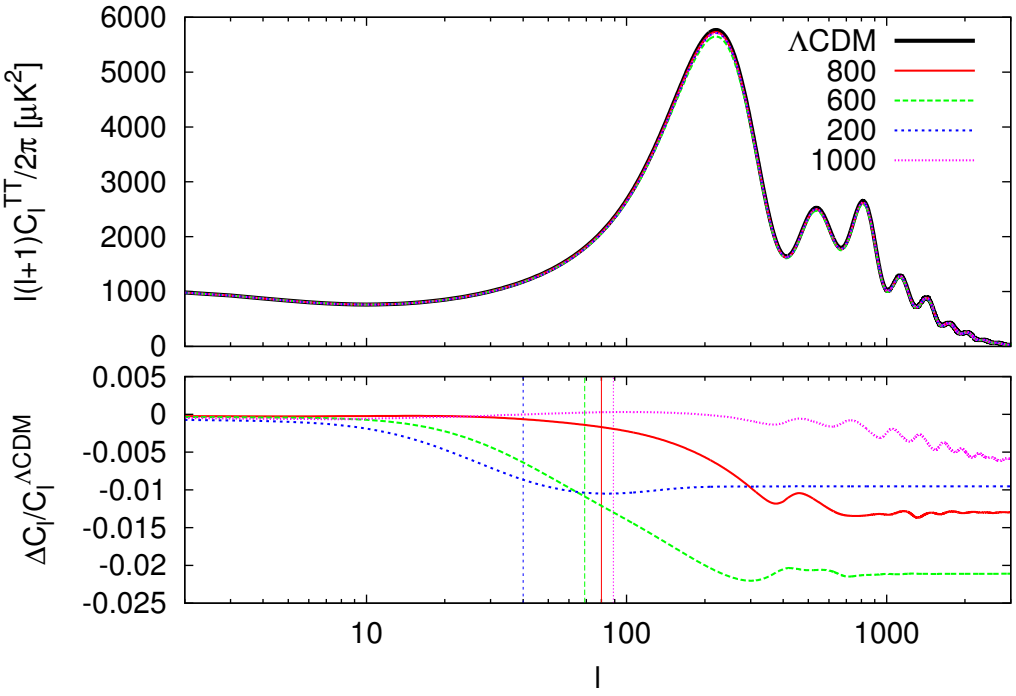

Figure 5.5: Temperature auto-correlation spectrum for four values of z_{TDS} and $\Delta z = 10^{-4}$. Vertical lines correspond to the characteristic angular moments l_{TDS} for each z_{TDS}.

full reionization at $z \sim 10$. As predicted, we observe a stronger polarization signal from large angular scales than l_{TDS}. In particular, for smaller values of z_{TDS}, the residual ionized fraction is larger and the rise of the C_l^E is larger.

Finally, we show the C_l^E including the late-time reionization in figure 5.7. We observe the small increase, except that the TDS effect is diluted by the full reionization for $l \lesssim l_{reio}$. This reionization is typically modeled as a hyperbolic tangent function. As it reaches the full ionized fraction, the TDS x_e asymptotically converges to the same value and the $\Delta C_l^E \to 0$ for small l.

5.4.3 Degeneracy with late-time reionization

Although the TDS and the late-time reionization have the same sort of implications on the spectra, we notice that the characteristic angular moment l_{TDS} sets a clear distinction between the two effects. For a fixed damping factor, the TDS signal becomes harder to distinguish as $z_{TDS} \to z_{reio}$. However, this was already expected

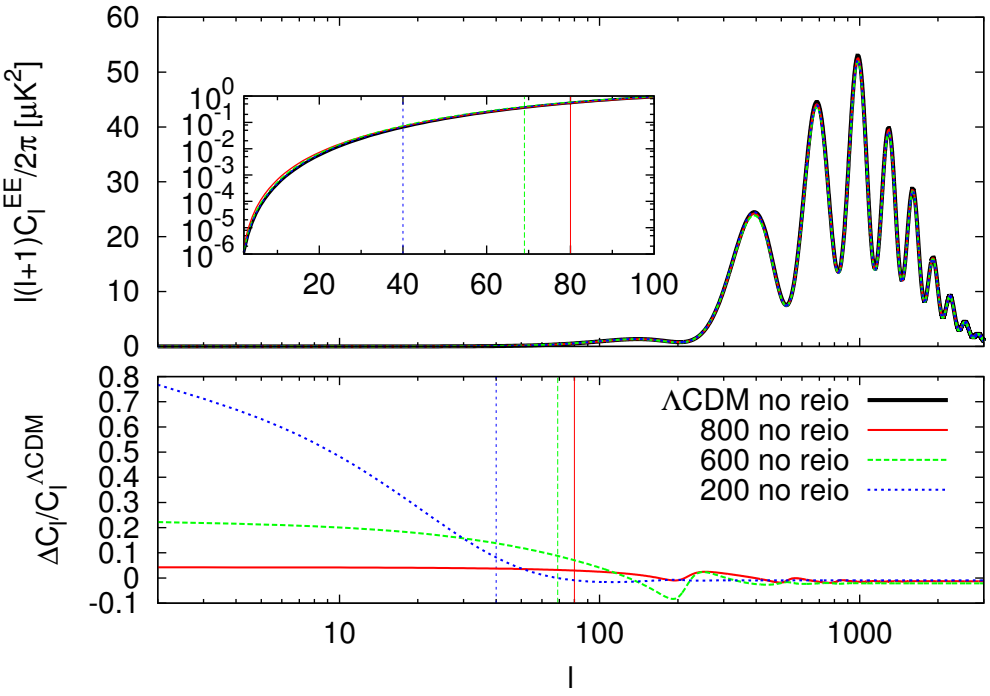

Figure 5.6: Polarization auto-correlation spectrum without full reionization for three values of z_{TDS} and $\Delta z = 10^{-4}$. Vertical lines correspond to the characteristic angular moments l_{TDS} for each z_{TDS}.

without the late-time reionization since the TDS optical depth is becomes small as z decreases for $z \lesssim 200$. Therefore, the region of parameter space that would be degenerate with late-reionization *a priori* has a faint signal and CMB experiments are insensitive to it.

The physics of late-reionization is still unknown and its cosmological modeling can take multiple forms. We will see in chapter 6 that the region of parameter space that can be probed with the CMB experiments does not encompass late-time reionization redshifts. Therefore, we expect the TDS sensitivity to be unaffected by the late-time reionization modeling.

5.4.4 Spatial variation of Q

The example of theoretical frameworks mentioned in section 3.1 also allow a spatial variation of constants which can have different effects on the CMB. For example, a spatial variation of α_{em} primarily diminishes the amplitude of the peaks and troughs

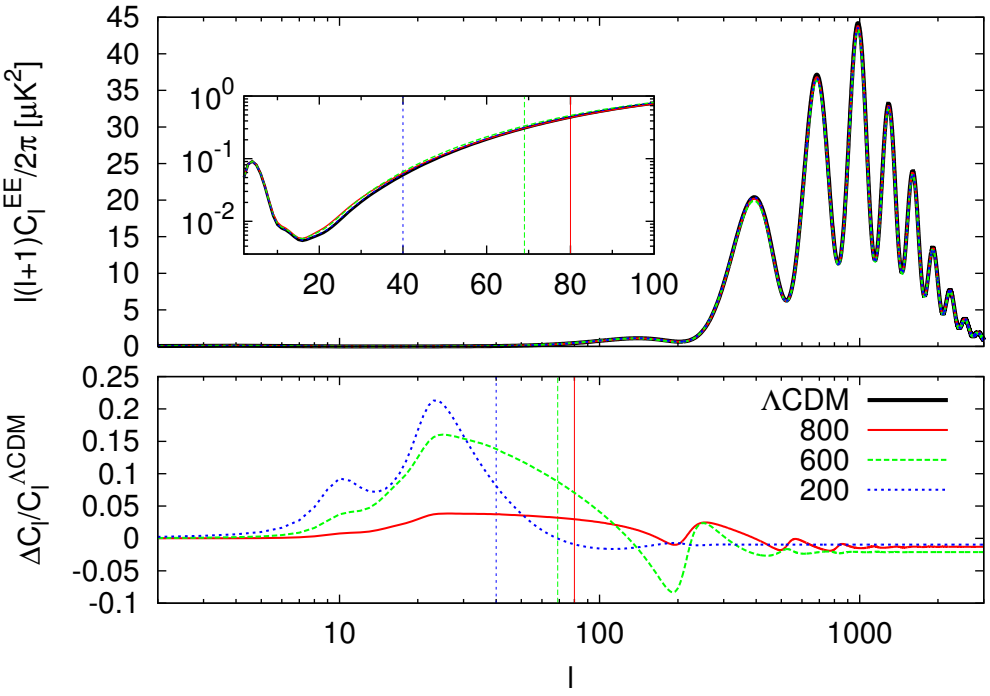

Figure 5.7: Polarization auto-correlation spectrum for three values of z_{TDS} and $\Delta z = 10^{-4}$. Vertical lines correspond to the characteristic angular moments l_{TDS} for each z_{TDS}.

in the power spectra, in addition of generator BB polarization and higher order spectra [46]. In our case, a spatial variation of z_{TDS} across the sky would act as a patchy reionization which can slightly modify the large l information [101] and potentially be further constrained than our homogeneous model.

Chapter 6

Detectability, Present Constraints and Forecast

With the modified CMB anisotropies in hand, we need to compare the effects with experimental data to determine the detectability of the TDS and impose constraints on the parameters of the scenario. We use the code MontePython [102], which scans the parameter space through Monte Carlo Markov Chains with a Metropolis-Hastings algorithm (see for eg. [103]) and compares the points with the experimental data of our choice to obtain the posterior Probability Distribution Function (PDF).

The strategy behind the parameter extraction from MontePython uses a Bayesian framework (see [104] for a review of Bayes statistics in cosmology). An effective chi-square for each set of experimental data is defined through

$$\chi^2_{\rm eff} \propto -2 \ln \mathcal{L}(\theta|{\rm data}), \tag{6.1}$$

where $\mathcal{L}(\theta|{\rm data})$ is the likelihood of a theory with parameters θ to the experimental results. For a given set of experimental data, $\chi^2_{\rm eff}$ permits a comparison of different points in the parameter space and the definition of meaningful bounds on the allowed region.

In the following sections, we choose to sample a cosmology with 6 varying ΛCDM parameters $\{\omega_b, \omega_{cdm}, n_s, A_s, h, z_{reio}\}$, in addition to our two TDS free parameters $\{z_{\rm TDS}, \Delta z\}$. We assume flat priors on all parameters and restrict the TDS parameter

space to

$$\begin{aligned} 30 \leq & z_{\rm TDS} \leq 1200, \\ 10^{-5} \leq & \ \Delta z \leq 10^{3}, \\ & \Delta z \leq z_{\rm TDS}. \end{aligned} \tag{6.2}$$

The range of z_{TDS} and the upper bound on Δz are selected to test only regions that are potentially observable (*i.e.* the change in the anisotropy spectra is more than 1 part in 1000). The lower bound on Δz is set where the asymptotic behaviour of instantaneous change in Q as been reached and $\Delta z \leq z_{\rm TDS}$ is needed for the requirement $Q(\text{now}) = Q_{\rm SM}$.

6.1 Detectability from WMAP and SPT

Firstly, we compare the TDS power spectra with the available anisotropy spectra data. We use the joint observations from the WMAP 7-year analysis [105] and the SPT [12] which together cover the TT spectrum to $l = 3000$. The WMAP7 polarization dataset only comprises the TE spectrum for moments up to $l = 1200$. Since we are using two complementary sets of data, the total effective chi-square is the sum of the individual ones

$$\chi^2_{\rm tot-eff} = \chi^2_{\rm WMAP-eff} + \chi^2_{\rm SPT-eff}. \tag{6.3}$$

The results in shown in figure 6.1, in the form a triangle plot, where each 2D subplot shows the PDF marginalized over all other parameters. The 1D subplots show the PDF of that single parameter, again marginalized over all other variables. The last three parameters are nuisance parameters that are used in the SPT likelihood to remove foreground systematics. Following the guidelines from the SPT collaboration [12], gaussian priors have been assigned to each of them. The results for the ΛCDM parameters are summarized in table 6.1 and are agreement with the values from the SPT collaboration (see table 3 in ref. [12]).

	$100\ \omega_b$	ω_{cdm}	n_s	$10^{+9}A_s$	h	z_{reio}
WMAP7+SPT	$2.231^{+0.042}_{-0.044}$	$0.1119^{+0.0047}_{-0.0051}$	$0.9627^{+0.011}_{-0.011}$	$2.454^{+0.099}_{-0.11}$	$0.7082^{+0.021}_{-0.023}$	$10.36^{+1.2}_{-1.2}$
Planck	$2.331^{+0.014}_{-0.015}$	$0.1179^{+0.0013}_{-0.0013}$	$0.957^{+0.0037}_{-0.0037}$	$2.432^{+0.039}_{-0.038}$	$0.7138^{+0.0059}_{-0.006}$	$11.39^{+0.39}_{-0.42}$

Table 6.1: Constraints on the ΛCDM parameters marginalized over the TDS parameters.

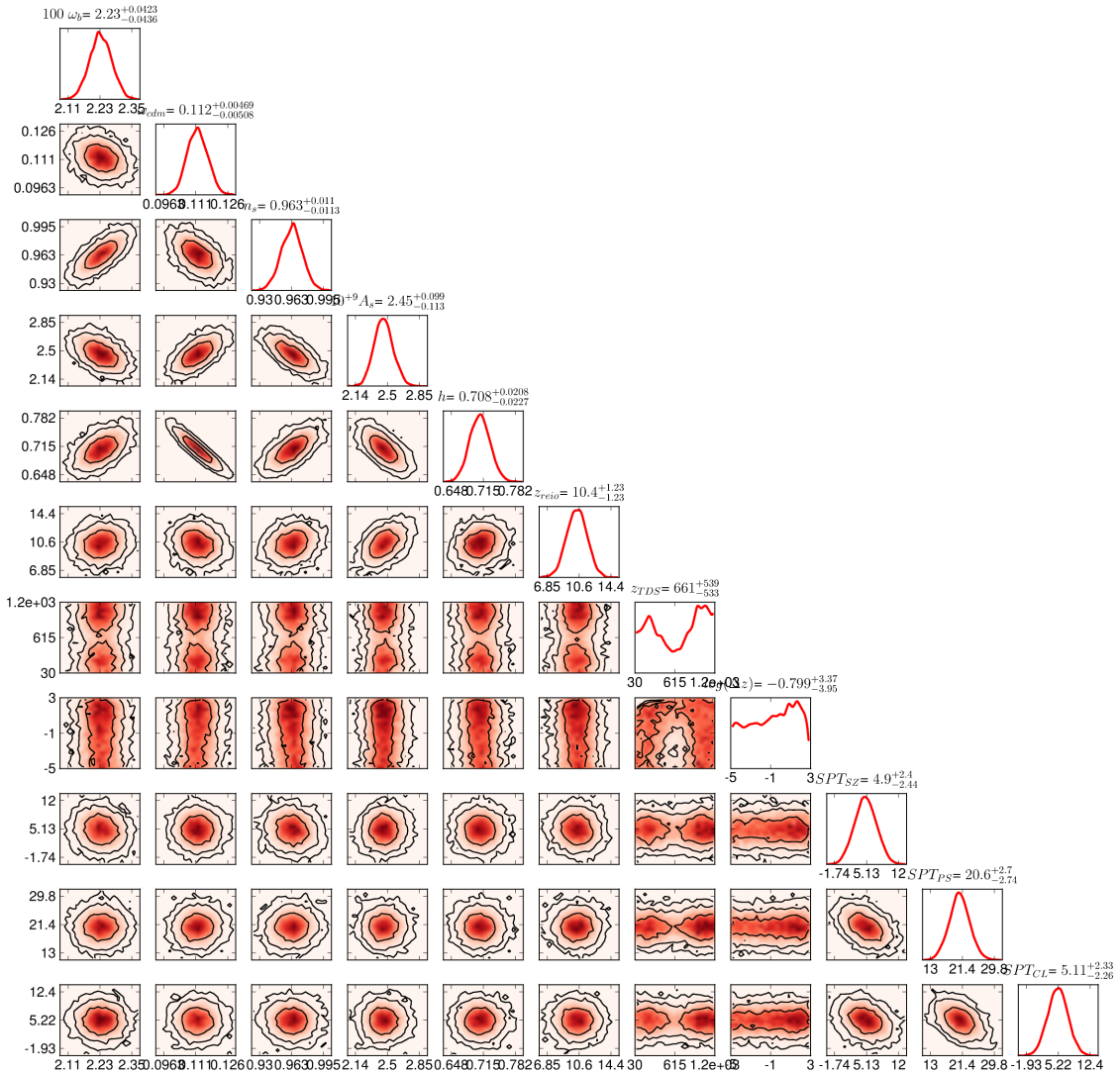

Figure 6.1: Triangle plot of the TDS compared to the WMAP7 and SPT datasets. The contour lines show the 68%, 95% and 99.7% confidence levels. The last three parameters are nuisance variables included in the SPT likelihood.

The TDS parameters are strongly correlated and we focus our attention on the 2D PDF between $z_{\rm TDS}$ and Δz rather than their individual 1D PDF. Since the posterior is not gaussian, the MCMC algorithm is not as efficient in exploring the PDF and renders a noisier plot. Fortunately, the support of the PDF is connected and the Metropolis-Hastings algorithm guaranties a correct estimate of the PDF [103]. We show the 1-sigma and 2-sigma confidence levels (CL) as the red curves in figure 6.2,

where we have taken the innermost shell on each sigma level to show conservative limits. We see that the highest likelihood lies around the regions where $z_{\rm TDS} < 200$, $z_{\rm TDS} > 900$ or $\Delta z > 10$, which all tend to the same phenomenology as the ΛCDM cosmology. Without strongly ruling out some parameter space, we find that the combined WMAP7 and SPT datasets have the resolution to disfavor the parameters yielding a large damping of C_l tail (see figure 5.4) at the 2-σ confidence level.

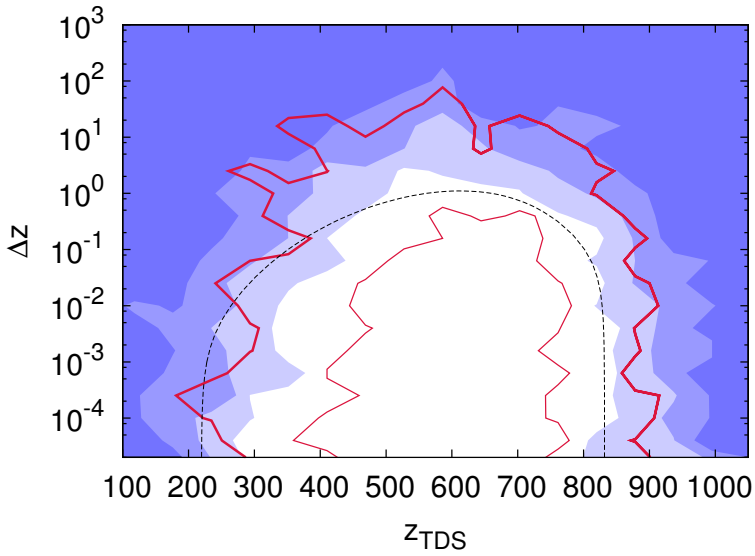

Figure 6.2: Contours of confidence level on the TDS parameters. The blue regions (from dark to pale) correspond to 68%, 95% and 99.7% CL on the Planck forecast and the red curves are the 68% and 95% CL using the WMAP7 + SPT data. The black curve shows the 1% damping factor from figure 5.4.

6.2 Forecast for Planck

The Planck satellite collaboration is set to publish their first set of data in early 2013. Until we can confront extensions of the ΛCDM to their results, we can at least forecast the detectability of our model by generating a set of mock data that emulates the design performance of the instruments.

The idea [106] is to add an experimental noise contribution n_{lm} to the multipole moments

$$a^X_{lm} = s^X_{lm} + n^X_{lm}, \tag{6.4}$$

where s_{lm} is the CMB signal contribution. For an experiment with known sensitivity

and beam width, the noise power spectrum can be modeled as

$$N_l^{XX'} \equiv \left\langle n_{lm}^{X*} n_{lm}^{X'} \right\rangle = \delta_{XX'} \theta_{\rm fwhm}^2 \sigma_X^2 \exp\left[l(l+1) \frac{\theta_{\rm fwhm}^2}{8 \ln 2} \right], \tag{6.5}$$

with the full width half maximum of the gaussian beam $\theta_{\rm fwhm}$ and the root mean square of instrumental noise σ_X. One can then generate artificial data with the appropriate noise characteristics.

We consider the three best high frequency channels listed in the Planck Scientific Programme [19] and produce a set of synthetic data around a fiducial cosmology with the best-fit parameters from WMAP7 using MontePython. The resulting triangle plot is shown in figure 6.3 and the contour lines of the $z_{\rm TDS} - \Delta z$ 2D PDF are drawn in shades of blue in figure 6.2.

We find that Planck has a much better ability to set constraints on the TDS parameters. In particular, a large portion of the parameter space (for $300 \lesssim z_{\rm TDS} \lesssim 850$ and $\Delta z \lesssim 1$) can be rejected at 99.7% CL. A quick comparison of the CL and damping factor contour lines in figure 6.2 illustrates the limiting factors in the sensitivity to the TDS. We find the high values of $z_{\rm TDS}$ for the same damping factor are experimentally easier to constrain. Some CL contour lines are outside the 1% damping marker for high $z_{\rm TDS}$ and their equivalent for low $z_{\rm TDS}$ are well inside. This shows that the experiments are not only sensitive to the amount of CMB anisotropies information loss in the extra Coulomb collisions due to the TDS partial reionization, but also to the redshift at which the energy is injected in the IGM. A low $z_{\rm TDS}$ corresponds to a small characteristic angular moment $l_{\rm TDS}$, which has a weaker statistically weight due to cosmic variance and consequently is harder to probe experimentally.

A comparison of the 1D PDF forecast for Planck to the PDF from WMAP7 + SPT is shown in figure 6.4. The sensitivity of Planck in clearly noticeable, even on the TDS parameters. The middle valley in $z_{\rm TDS}$ is significantly deeper and wider, while the PDF of Δz falls off more rapidly as it decreases.

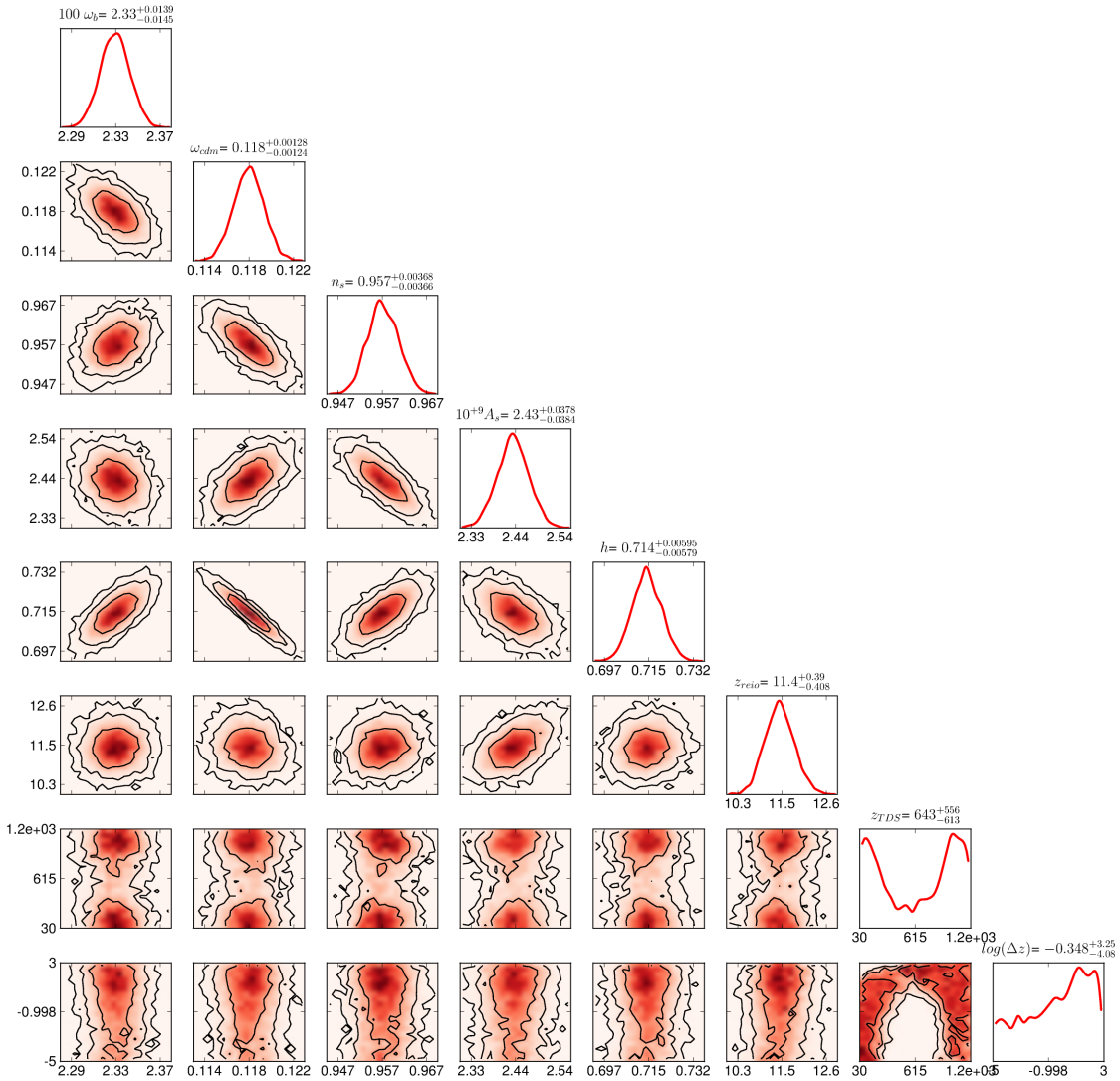

Figure 6.3: Triangle plot of the TDS forecast on Planck-like emulated data. The contour lines show the 68%, 95% and 99.7% confidence levels.

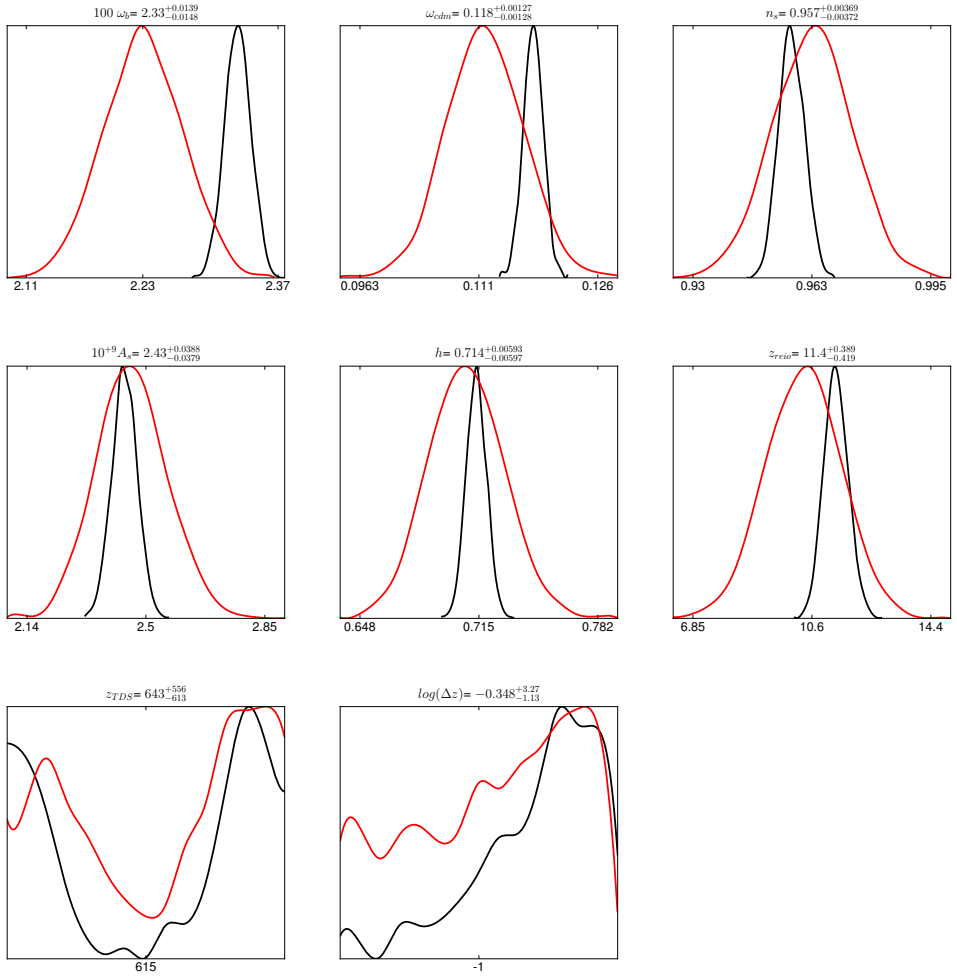

Figure 6.4: 1D PDF of the cosmological parameters from WMAP7 + SPT (red) and forecast for Planck (black).

Chapter 7

Conclusions

An experimental observation of the variation of a fundamental constant would provide valuable information on the possible extensions of the Standard Model. On the other hand, rigorous tests of their constancy over time and space can also constrain new physics. A large class of probes at different cosmological epochs have already been studied in the literature, all of which are consistent with no variation to various degrees of precision. In particular, the present constraints at the CMB emission are of the $\mathcal{O}(1\%)$ and come from studies that neglected new physics in the nuclear sector of the recombination process.

We investigate in new probe of VFC, where the ionization history of the Universe is modified through the emission of electrons arising from the beta decay of tritium. The TDS can be realized if the Q-value of the reaction is initially negative, which happens through the variation of a combination of constants and is viable under the present bounds.

We model the variation of Q with two parameters, the transitional epoch $z_{\rm TDS}$ and the timescale of the transition Δz. We found that the ionization history is more strongly modified for $z_{\rm TDS}$ centered at 600 with a damping of the tail of the C_l of the order of 3% and a significant rise in the low l polarization signal.

We confront the TDS with CMB data from WMAP 7-year analysis and the SPT. The results show no sign of deviations from the ΛCDM cosmology, with maximal likelihood for no modification in the power spectra. The present data can already constrain a region of TDS parameter space at 2σ CL. We forecast the sensibility of Planck and find that it will probe a larger section of the parameter space, potentially ruling out a significant region at the 3σ CL. In the excluded region, the limits correspond to constraints on the nucleon and electron masses shown in figure 7.1. The

dark blue section is excluded if we consider a TDS starting at $Q = -15$ keV just before $z_{\rm TDS}$ (recall from eq. 4.28 that we need this Q-value at He recombination for a full accumulation of T) and the pale region is excluded for a TDS starting at $Q = 0$ keV.

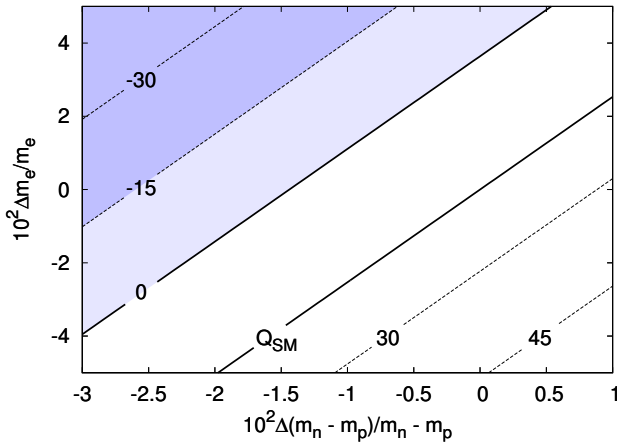

Figure 7.1: Contour lines of Q in keV for a variation in the nucleon and electron masses. The shaded region allows is excluded from the TDS and CMB data around $z \sim 600$ for fast transition $\Delta z \to 0$ if we assume a $Q = -15$ keV (dark) or $Q = 0$ keV (pale) at $z_{\rm TDS}$.

In light of this project, we see that changes (that are allowed under present constraints) in the nuclear sector of the recombination process can alter the cosmology to a detectable level. With the ever-increasing precision in observational data, the TDS provides an extra probe of VFC which should be considered in the full battery of VFC cosmological tests.

Appendix A

Decay Rates

We give more details on the derivation of the decay rates with variable excess energy presented in section 3.4.

A.1 Tritium → Helium-3

This decay happens via beta decay through the reaction $\mathrm{T} \to {}^3\mathrm{He} + e^- + \bar{\nu}$, shown in figure 3.2. Our derivation is based on ref. [107]. Assuming the mass of the W boson is much greater than the momentum transferred and a vertex factor of the form $V_{ud}\gamma^\mu(g_v - g_a\gamma^5)$ between T, He and W, the decay rate is given by

$$\mathrm{d}\Gamma = 16G_F^2V_{ud}^2F(2,E_e)\frac{(2\pi)^4\delta^{(4)}(p_\mathrm{T} - p_\mathrm{He} - p_e - p_\nu)}{16E_\mathrm{T}E_\mathrm{He}E_eE_\nu}\frac{\mathrm{d}^3\mathbf{p}_\mathrm{He}}{(2\pi)^3}\frac{\mathrm{d}^3\mathbf{p}_e}{(2\pi)^3}\frac{\mathrm{d}^3\mathbf{p}_\nu}{(2\pi)^3}\times \tag{A.1}$$

$$\times\left[(g_v+g_a)^2(p_\mathrm{T}\cdot p_\nu)(p_\mathrm{He}\cdot p_e) + (g_v-g_a)^2(p_\mathrm{T}\cdot p_e)(p_\mathrm{He}\cdot p_\nu)\right. \tag{A.2}$$

$$\left.+(g_a^2-g_v^2)m_\mathrm{T}m_\mathrm{He}(p_e\cdot p_\nu)\right] \tag{A.3}$$

$$= F(2,E_e)\frac{G_F^2V_{ud}^2}{(2\pi)^5}\frac{\mathrm{d}^3\mathbf{p}_e}{E_\mathrm{T}E_e}\left\{p_{\mathrm{T}\sigma}p_{e\rho}\left[(g_v+g_a)^2(A_{\mathrm{He},\nu})^{\sigma\rho} + (g_v-g_a)^2\eta^{\sigma\rho}\eta_{\alpha\beta}(A_{\mathrm{He},\nu})^{\alpha\beta}\right]\right. \tag{A.4}$$

$$\left.+p_{e\sigma}(g_a^2-g_v^2)m_\mathrm{T}m_\mathrm{He}(B_\nu)^\sigma\right\}, \tag{A.5}$$

where in the second equality we have only explicitly kept the integral over the outgoing electron and defined

$$(A_{\mathrm{He},\nu})^{\sigma\rho} \equiv \int \frac{\mathrm{d}^3\mathbf{p}_{\mathrm{He}}\mathrm{d}^3\mathbf{p}_\nu}{E_{\mathrm{He}}E_\nu}\delta^{(4)}(Z - p_{\mathrm{He}} - p_\nu)p^\sigma_{\mathrm{He}}p^\rho_\nu \tag{A.6}$$

$$= \frac{C\eta^{\sigma\rho}}{3}\left[(p_{\mathrm{He}}\cdot p_\nu) - \frac{(Z\cdot p_{\mathrm{He}})(Z\cdot p_\nu)}{Z^2}\right] \tag{A.7}$$

$$- \frac{CZ^\sigma Z^\rho}{3Z^2}\left[(p_{\mathrm{He}}\cdot p_\nu) - \frac{4(Z\cdot p_{\mathrm{He}})(Z\cdot p_\nu)}{Z^2}\right], \tag{A.8}$$

$$(B_\nu)^\sigma \equiv \int \frac{\mathrm{d}^3\mathbf{p}_{\mathrm{He}}\mathrm{d}^3\mathbf{p}_\nu}{E_{\mathrm{He}}E_\nu}\delta^{(4)}(Z - p_{\mathrm{He}} - p_\nu)p^\sigma_\nu \tag{A.9}$$

$$= \frac{Z\cdot p_\nu}{Z^2}CZ^\sigma \tag{A.10}$$

$$F(Z,E) = 2(1+\gamma)\frac{|\Gamma(\gamma + i\alpha Z\frac{E}{p})|^2}{[\Gamma(2\gamma+1)]^2}(2p\sqrt{\frac{5}{3}}R)^{2(\gamma-1)}\mathrm{e}^{\pi\alpha Z\frac{E}{p}}, \tag{A.11}$$

with $\gamma = \sqrt{1-(\alpha Z)^2}$. The integrals A and B where found by contracting with $Z^\sigma \equiv (p_{\mathrm{T}} - p_E)^\sigma$ and $\eta^{\sigma\rho}$ and $F(Z,E)$ is the Coulomb correction factor [57] accounting for the attraction of the emitted electrons with the nucleus. The resulting terms depend only on the integral

$$C \equiv \int \frac{\mathrm{d}^3\mathbf{p}_{\mathrm{He}}\mathrm{d}^3\mathbf{p}_\nu}{E_{\mathrm{He}}E_\nu}\delta^{(4)}(Z - p_{\mathrm{He}} - p_\nu) = \frac{4\pi m_{\mathrm{T}}}{Z^2}(E_e^{max} - E_e), \tag{A.12}$$

where $E_e^{max} = \frac{1}{2m_{\mathrm{T}}}(m_{\mathrm{T}}^2 + m_e^2 - m_{\mathrm{He}}^2)$ is the maximal relativistic energy of the outgoing electron, found with the 4-momenta relationship $(p_{\mathrm{T}} - p_e)^2 = (p_{\mathrm{He}} + p_\nu)^2$ in the tritium rest frame. Putting all of this together and using the approximations

$$\frac{m_{\mathrm{T}}}{m_{\mathrm{He}}} \simeq 1 \qquad\qquad E_e^{max} \ll m_{\mathrm{T}} \tag{A.13}$$

and rewriting $\mathrm{d}^3\mathbf{p}_e$ in terms of $\mathrm{d}E_e$, we find

$$\frac{\mathrm{d}\Gamma}{\mathrm{d}E_e} = \frac{(G_F V_{ud})^2}{2\pi^3}F(2,E_e)(g_v^2 + 3g_a^2)E_e p_e(E_e^{max} - E_e)^2 \tag{A.14}$$

Finally, we assume that the kinetic energy of the electron is much smaller than its rest mass ($Q \ll m_e$) and use the nonrelativistic approximation $E_e^{max} = m_e + Q$ to

find the decay rate of tritium.

$$\Gamma_{\mathrm{T}\to\mathrm{He}}(Q) = \frac{(G_F V_{ud})^2}{2\pi^3}(g_v^2 + 3g_a^2)\int_{m_e}^{m_e+Q} \mathrm{d}E\, F(2,E)E\sqrt{E^2-m_e^2}(Q+m_e-E)^2 \tag{A.15}$$

This is equation 3.16 used in the text and agrees with both refs. [107] and [108] in the case of massless neutrinos. Using the known values of $Q = 18.59$ keV, the half-life of tritium 12.32 years and the helium-3 radius of $R = 9.885 \times 10^{-6}$ keV^{-1} [109], we find

$$g_a = 1.239. \tag{A.16}$$

In ref. [107], the authors obtain a value of $g_a = 1.247$. We note that g_a may also change as a result of VFC. However, from A.15 we see that its effect is much smaller than a variation of Q and can be safely neglected.

A.2 Helium-3 $\to$ Tritium

The decay of helium-3 into tritium is possible (energy constraints permitting) through electron capture. Using the same vertex forms as above, we find a spin-averaged amplitude of

$$\langle|\mathcal{M}|^2\rangle = 8G_F^2V_{ud}^2\left[(g_v+g_a)^2(p_{\mathrm{T}}\cdot p_\nu)(p_{\mathrm{He}}\cdot p_e) + (g_v-g_a)^2(p_{\mathrm{T}}\cdot p_e)(p_{\mathrm{He}}\cdot p_\nu)\right. \tag{A.17}$$

$$\left.+(g_a^2-g_v^2)m_{\mathrm{T}}m_{\mathrm{He}}(p_e\cdot p_\nu)\right]. \tag{A.18}$$

We take the approximation that the electron and helium-3 are at rest and neglect the recoil of tritium. Then the only particle with kinetic energy is the neutrino with 4-momentum

$$p_\nu = (\tilde{Q},\tilde{Q},0,0), \tag{A.19}$$

because all excess energy goes in the neutrino in this approximation. We name the excess energy of this reaction $\tilde{Q} > 0$, to distinguish the sign with the excess energy in the opposite reaction ($\tilde{Q} = -Q$). The spin-averaged amplitude is then

$$\langle|\mathcal{M}|^2\rangle = 8G_F^2V_{ud}^2m_{\mathrm{T}}m_{\mathrm{He}}m_e\tilde{Q}(g_v^2+3g_a^2). \tag{A.20}$$

The differential cross section is

$$\frac{\mathrm{d}\sigma}{\mathrm{d}\Omega} = \frac{1}{(8\pi)^2}\frac{\langle|\mathcal{M}|^2\rangle}{(E_e+E_{\mathrm{He}})^2}\frac{|\mathbf{p_f}|}{|\mathbf{p_i}|} \tag{A.21}$$

$$= \frac{G_F^2 V_{ud}^2}{8\pi^2}\frac{m_{\mathrm{T}} m_{\mathrm{He}} m_e \tilde{Q}^2(g_v^2+3g_a^2)}{(m_e+m_{\mathrm{He}})^2 m_e v}, \tag{A.22}$$

where we took the final 3-momentum to be $\tilde{Q}$ and initial to be $m_e v$. The cross section is then

$$\sigma = \frac{G_F^2 V_{ud}^2}{2\pi}\frac{m_{\mathrm{T}} m_{\mathrm{He}} \tilde{Q}^2(g_v^2+3g_a^2)}{(m_e+m_{\mathrm{He}})^2 v} \tag{A.23}$$

The decay rate is given by

$$\Gamma = v\sigma|\Psi(0)|^2 = \frac{G_F^2 V_{ud}^2}{8\pi^2}\tilde{Q}^2(g_v^2+3g_a^2)|\Psi(0)|^2, \tag{A.24}$$

where we again assumed $m_{\mathrm{T}} \sim m_{\mathrm{He}}$. The probability of finding one of the two electrons at the centre $|\Psi(0)|^2 = \langle\delta^{(3)}(\overrightarrow{r_1}) + \delta^{(3)}(\overrightarrow{r_2})\rangle$ cannot be done analytically. However, high precision experiments measuring the charge radius of atoms use the finite radius corrections to energy levels to relate energy shifts with the charge radius by [110]

$$\Delta E_{\mathrm{nuc}} = \frac{2\pi Z e^2 r_c^2}{3}|\Psi(0)|^2. \tag{A.25}$$

$|\Psi(0)|^2$ has therefore been calculated numerically to high accuracy in the context of these experiments and ref. [110] found a value of

$$|\Psi(0)|^2 = \frac{3\cdot 10.572}{4\pi\alpha c}\frac{\mathrm{MHz}}{\mathrm{fm}^2}, \tag{A.26}$$

for the ground state of helium. We find our final expression for the decay rate

$$\Gamma_{\mathrm{He}\to\mathrm{T}}(\tilde{Q}) = \frac{3\cdot 10.572}{8\pi^2}\frac{G_F^2 V_{ud}^2}{\alpha c}\tilde{Q}^2(g_v^2+3g_a^2)\frac{\mathrm{MHz}}{\mathrm{fm}^2} \tag{A.27}$$

or equivalently a lifetime of

$$\tau_{\mathrm{He}\to\mathrm{T}}(\tilde{Q}) = 2.05\times 10^5\,\mathrm{yr}\left(\frac{10\,\mathrm{keV}}{\tilde{Q}}\right)^2. \tag{A.28}$$

Appendix B

The Boltzmann equation

The Boltzmann equation tells us the abundance rate of change of a particular species when we know its creation and annihilation mechanisms. It simply corresponds to the rate of production of the species minus the rate of elimination, integrated over the possible momenta. If we consider the abundance of species 1, which interacts with species 2, 3 and 4 via the reversible reaction $1 + 2 \leftrightarrow 3 + 4$, the Boltzmann equation is [59]

$$a^{-3}\frac{\mathrm{d}(n_1 a^3)}{\mathrm{d}t} = \prod_{i=1}^{4}\left(\int \frac{\mathrm{d}^3 p_i}{(2\pi)^3 2E_i}\right)(2\pi)^4\delta^4(p_1+p_2-p_3-p_4)|\mathcal{M}|^2\times \\ \times\left\{f_3 f_4(1\pm f_1)(1\pm f_2) - f_1 f_2(1\pm f_3)(1\pm f_4)\right\}. \tag{B.1}$$

The left-hand side means that we are considering the rate of change of the number of particles of species 1 in a comoving volume, where a is the FRW scale factor. On the right-hand side, we have the integrals over all momenta of the species. The $2E$ factor comes from the fact that we really had to integrate of the 4-momenta, but since $E^2 = p^2 + m^2$, the integral over E is trivial using the delta function $\delta(E^2 - p^2 - m^2) = \delta(E - \sqrt{p^2+m^2})/2E$ and we get the corresponding factor in the denominator. The amplitude $\mathcal{M}$ squared is the probability of interaction, as a function of the incoming and outgoing momenta. The creation rate is also proportional to the number of particle of species 3 and 4, and annihilation proportional to the density of species 1 and 2. This is represented by the terms f_i in the curly bracket, where f_i is the Bose-Einstein or Fermi-Dirac distribution, depending on the nature of each species. The $(1 \pm f_i)$ terms correspond to Bose enhancement or Pauli blocking,

the + sign for the former and − the latter. They account for the fact that fermions don't want to be in the same state and bosons do, hence changing the probability of creating a particle in a specific state. Had the reaction not been reversible, the amplitude squared for each direction would have been multiplied to the corresponding creation or elimination factor in the bracket.

At high energies, which is the case in early universe, the distribution function simplifies

$$f \equiv \frac{1}{\mathrm{e}^{\frac{E-\mu}{T}} \pm 1} \xrightarrow{E-\mu \gg T} \mathrm{e}^{\frac{\mu}{T}} \mathrm{e}^{\frac{-E}{T}} \tag{B.2}$$

$$1 \pm f \longrightarrow 1 \tag{B.3}$$

and so the bracket term in equation B.1 reduces to

$$f_3 f_4 (1 \pm f_1)(1 \pm f_2) - f_1 f_2 (1 \pm f_3)(1 \pm f_4) \longrightarrow \mathrm{e}^{\frac{-(E_1+E_2)}{T}} \left(\mathrm{e}^{\frac{\mu_3+\mu_4}{T}} - \mathrm{e}^{\frac{\mu_1+\mu_2}{T}} \right). \tag{B.4}$$

The only free parameters at a given temperature on the left-hand side of equation B.1 are the chemical potentials μ_i which represent how much away from equilibrium the number of particle of species i is. If we consider the Boltzmann equation for each species in the reaction, we have a system of integro-differential equations, which we can solve to find $\mu_i(T)$. It is more natural to solve for the number density n_i, which is related to the chemical potential by the relation

$$n_i \equiv g_i \int \frac{\mathrm{d}^3 p}{(2\pi)^3} f_i = g_i \mathrm{e}^{\frac{\mu_i}{T}} \int \frac{\mathrm{d}^3 p}{(2\pi)^3} \mathrm{e}^{\frac{-E_i}{T}}, \tag{B.5}$$

where g_i is the number of degrees of freedom of the particle at a given energy. We made use of the approximation from equation B.2 in the last equality. We can express the chemical potential in a more compact way using the equilibrium value ($\mu_i = 0$) of the number density

$$n_i^{(0)} \equiv g_i \int \frac{\mathrm{d}^3 p}{(2\pi)^3} \mathrm{e}^{\frac{-E_i}{T}} = \begin{cases} g_i \left(\frac{m_i T}{2\pi}\right)^{\frac{2}{3}} \mathrm{e}^{\frac{-m_i}{T}} & m_i \gg T \\ g_i \frac{T^3}{\pi^2} & m_i \ll T. \end{cases} \tag{B.6}$$

Defining the thermally averaged cross section

$$\langle \sigma v \rangle \equiv \frac{1}{n_1^{(0)} n_2^{(0)}} \prod_{i=1}^{4} \left(\int \frac{\mathrm{d}^3 p_i}{(2\pi)^3 2E_i} \right) \mathrm{e}^{\frac{-(E_1+E_2)}{T}} (2\pi)^4 \delta^4 \left(p_1 + p_2 - p_3 - p_4\right) |\mathcal{M}|^2, \tag{B.7}$$

the Boltzmann equation becomes

$$a^{-3}\frac{\mathrm{d}\left(n_1 a^3\right)}{\mathrm{d}t} = n_1^{(0)} n_2^{(0)} \langle \sigma v \rangle \left\{ \frac{n_3 n_4}{n_3^{(0)} n_4^{(0)}} - \frac{n_1 n_2}{n_1^{(0)} n_2^{(0)}} \right\}. \tag{B.8}$$

In particular, when species 1 is in equilibrium, the left-hand side is 0 and we get the Saha equation

$$\frac{n_3 n_4}{n_1 n_2} = \frac{n_3^{(0)} n_4^{(0)}}{n_1^{(0)} n_2^{(0)}}, \tag{B.9}$$

where the number densities are given by equations B.5 and B.6.

Bibliography

[1] Jean-Philippe Uzan. Varying Constants, Gravitation and Cosmology. *Living Rev.Rel.*, 14:2, 2011.

[2] V.F. Mukhanov. *Physical Foundations of Cosmology*. Cambridge University Press, 2005.

[3] K Nakamura and Particle Data Group. Review of particle physics. *Journal of Physics G: Nuclear and Particle Physics*, 37(7A):075021, 2010.

[4] Takeshi Chiba. The Constancy of the Constants of Nature: Updates. *Prog.Theor.Phys.*, 126:993–1019, 2011.

[5] Richard H. Cyburt, Brian D. Fields, and Keith A. Olive. An Update on the big bang nucleosynthesis prediction for Li-7: The problem worsens. *JCAP*, 0811:012, 2008.

[6] Maxim Pospelov and Josef Pradler. Big Bang Nucleosynthesis as a Probe of New Physics. *Ann.Rev.Nucl.Part.Sci.*, 60:539–568, 2010.

[7] G. Gamow. Expanding universe and the origin of elements. *Phys. Rev.*, 70:572–573, Oct 1946.

[8] Ralph A. Alpher and Robert C. Herman. Remarks on the evolution of the expanding universe. *Phys. Rev.*, 75:1089–1095, Apr 1949.

[9] Arno A. Penzias and Robert Woodrow Wilson. A Measurement of excess antenna temperature at 4080-Mc/s. *Astrophys.J.*, 142:419–421, 1965.

[10] John C. Mather, E.S. Cheng, R.A. Shafer, C.L. Bennett, N.W. Boggess, et al. A Preliminary measurement of the Cosmic Microwave Background spectrum by the Cosmic Background Explorer (COBE) satellite. *Astrophys.J.*, 354:L37–L40, 1990.

[11] George F. Smoot, C.L. Bennett, A. Kogut, E.L. Wright, J. Aymon, et al. Structure in the COBE differential microwave radiometer first year maps. *Astrophys.J.*, 396:L1–L5, 1992.

[12] R. Keisler, C.L. Reichardt, K.A. Aird, B.A. Benson, L.E. Bleem, et al. A Measurement of the Damping Tail of the Cosmic Microwave Background Power Spectrum with the South Pole Telescope. *Astrophys.J.*, 743:28, 2011.

[13] Sudeep Das, Tobias A. Marriage, Peter A.R. Ade, Paula Aguirre, Mandana Amir, et al. The Atacama Cosmology Telescope: A Measurement of the Cosmic Microwave Background Power Spectrum at 148 and 218 GHz from the 2008 Southern Survey. *Astrophys.J.*, 729:62, 2011.

[14] C.L. Reichardt, P.A.R. Ade, J.J. Bock, J. Richard Bond, J.A. Brevik, et al. High resolution CMB power spectrum from the complete ACBAR data set. *Astrophys.J.*, 694:1200–1219, 2009.

[15] J.L. Sievers, B.S. Mason, L. Weintraub, C. Achermann, P. Altamirano, et al. Cosmological Results from Five Years of 30 GHz CMB Intensity Measurements with the Cosmic Background Imager. 2009.

[16] Clive Dickinson, Richard A. Battye, Pedro Carreira, Kieran Cleary, Rod D. Davies, et al. High sensitivity measurements of the CMB power spectrum with the extended Very Small Array. *Mon.Not.Roy.Astron.Soc.*, 353:732, 2004.

[17] William C. Jones, P. Ade, J. Bock, J. Bond, J. Borrill, et al. A Measurement of the angular power spectrum of the CMB temperature anisotropy from the 2003 flight of BOOMERANG. *Astrophys.J.*, 647:823–832, 2006.

[18] D.N. Spergel et al. First year Wilkinson Microwave Anisotropy Probe (WMAP) observations: Determination of cosmological parameters. *Astrophys.J.Suppl.*, 148:175–194, 2003.

[19] The Scientific Programme of Planck. 2006.

[20] F. W. Dyson, A. S. Eddington, and C. Davidson. A determination of the deflection of light by the sun's gravitational field, from observations made at the total eclipse of may 29, 1919. *Philosophical Transactions of the Royal Society of London. Series A, Containing Papers of a Mathematical or Physical Character*, 220(571-581):291–333, 1920.

[21] R.M. Wald. *General Relativity*. Physics/Astrophysics. University of Chicago Press, 1984.

[22] D. Larson, J. Dunkley, G. Hinshaw, E. Komatsu, M.R. Nolta, et al. Seven-Year Wilkinson Microwave Anisotropy Probe (WMAP) Observations: Power Spectra and WMAP-Derived Parameters. *Astrophys.J.Suppl.*, 192:16, 2011.

[23] Paul A.M. Dirac. The Cosmological constants. *Nature*, 139:323, 1937.

[24] P. A. M. Dirac. A New Basis for Cosmology. *Royal Society of London Proceedings Series A*, 165:199–208, April 1938.

[25] P. Jordan. Relativistische gravitationstheorie mit variabler gravitationskonstante. *Naturwissenschaften*, 33:250–251, 1946. 10.1007/BF01204481.

[26] C. Brans and R. H. Dicke. Mach's principle and a relativistic theory of gravitation. *Phys. Rev.*, 124:925–935, Nov 1961.

[27] Yasunori Fujii and Kei ichi Maeda. Cambridge University Press, 2003.

[28] Jacob D. Bekenstein. Fine-structure constant: Is it really a constant? *Phys. Rev. D*, 25:1527–1539, Mar 1982.

[29] Keith A. Olive and Maxim Pospelov. Evolution of the fine structure constant driven by dark matter and the cosmological constant. *Phys.Rev.*, D65:085044, 2002.

[30] T. Damour and Alexander M. Polyakov. The String dilaton and a least coupling principle. *Nucl.Phys.*, B423:532–558, 1994.

[31] The international system of units (si). Technical report, Paris, 2008.

[32] A. Godone, C. Novero, P. Tavella, and K. Rahimullah. New experimental limits to the time variations of g(p) (m(e) / m(p and alpha. *Phys.Rev.Lett.*, 71:2364–2366, 1993.

[33] A. I. Shlyakhter. Direct test of the constancy of fundamental nuclear constants. *Nature*, 264:340, November 1976.

[34] RH Dicke. Dirac's cosmology and the dating of meteorites. 1959.

[35] MP Savedoff. Physical constants in extra-galactic nebulae. 1956.

[36] M. Livio, D. Hollowell, A. Weiss, and J.W. Truran. The anthropic significance of the existence of an excited state of 12 c. *Nature*, 340(6231):281–284, 1989.

[37] H. Oberhummer, A. Csoto, and H. Schlattl. Stellar production rates of carbon and its abundance in the universe. *Science*, 289(5476):88–90, 2000.

[38] Rishi Khatri and Benjamin D. Wandelt. 21 cm radiation: A new probe of variation in the fine structure constant. *Phys.Rev.Lett.*, 98:111301, 2007.

[39] Manoj Kaplinghat, Robert J. Scherrer, and Michael S. Turner. Constraining variations in the fine structure constant with the cosmic microwave background. *Phys.Rev.*, D60:023516, 1999.

[40] Edward W. Kolb, Malcolm J. Perry, and T. P. Walker. Time variation of fundamental constants, primordial nucleosynthesis, and the size of extra dimensions. *Phys. Rev. D*, 33:869–871, Feb 1986.

[41] Michael T. Murphy, J.K. Webb, and V.V. Flambaum. Further evidence for a variable fine-structure constant from Keck/HIRES QSO absorption spectra. *Mon.Not.Roy.Astron.Soc.*, 345:609, 2003.

[42] J.K. Webb, J.A. King, M.T. Murphy, V.V. Flambaum, R.F. Carswell, et al. Indications of a spatial variation of the fine structure constant. *Phys.Rev.Lett.*, 107:191101, 2011.

[43] Kim Griest, Jonathan B. Whitmore, Arthur M. Wolfe, J. Xavier Prochaska, J. Christopher Howk, et al. Wavelength Accuracy of the Keck HIRES Spectrograph and Measuring Changes in the Fine Structure Constant. *Astrophys.J.*, 708:158–170, 2010.

[44] Julian A. King, John K. Webb, Michael T. Murphy, Victor V. Flambaum, Robert F. Carswell, et al. Spatial variation in the fine-structure constant – new results from VLT/UVES. 2012.

[45] Ewan Cameron and Tony Pettitt. On the Evidence for Cosmic Variation of the Fine Structure Constant: A Bayesian Reanalysis of the Quasar Dataset. 2012.

[46] Kris Sigurdson, Andriy Kurylov, and Marc Kamionkowski. Spatial variation of the fine - structure parameter and the cosmic microwave background. *Phys.Rev.*, D68:103509, 2003.

[47] Richard A. Battye, Robert Crittenden, and Jochen Weller. Cosmic concordance and the fine structure constant. *Phys.Rev.*, D63:043505, 2001.

[48] P.P. Avelino, C.J.A.P. Martins, G. Rocha, and Pedro T.P. Viana. Looking for a varying alpha in the cosmic microwave background. *Phys.Rev.*, D62:123508, 2000.

[49] G. Rocha, R. Trotta, C.J.A.P. Martins, A. Melchiorri, P.P. Avelino, et al. Measuring alpha in the early universe: cmb polarization, reionization and the fisher matrix analysis. *Mon.Not.Roy.Astron.Soc.*, 352:20, 2004.

[50] Kazuhide Ichikawa, Toru Kanzaki, and Masahiro Kawasaki. CMB constraints on the simultaneous variation of the fine structure constant and electron mass. *Phys.Rev.*, D74:023515, 2006.

[51] Petruta Stefanescu. Constraints on time variation of fine structure constant from WMAP-3yr data. *New Astron.*, 12:635–640, 2007.

[52] Claudia G. Scoccola, Susana J. Landau, and Hector Vucetich. WMAP 5-year constraints on time variation of α and m_e. 2009.

[53] Susana.J. Landau and Claudia G. Scoccola. Constraints on variation in α and m_e from WMAP 7-year data. *Astron.Astrophys.*, 517:A62, 2010.

[54] Kenneth S. Krane. *Introductory Nuclear Physics*. John Wiley and Sons, 1988.

[55] J. Gasser and H. Leutwyler. Quark masses. *Physics Reports*, 87(3):77 – 169, 1982.

[56] Andre Walker-Loud, Carl E. Carlson, and Gerald A. Miller. The Electromagnetic Self-Energy Contribution to $M_p - M_n$ and the Isovector Nucleon Magnetic Polarizability. *Phys.Rev.Lett.*, 108:232301, 2012.

[57] A. Bottino and G. Ciocchetti. Coulomb corrections to nuclear beta decay. *Physics Letters B*, 43(3):170–174, 1973.

[58] Daniel Baumann. TASI Lectures on Inflation. 2009.

[59] Scott Dodelson. *Modern Cosmology*. Academic Press, 1 edition, March 2003.

[60] Alain Coc and Elisabeth Vangioni. Big-bang nucleosynthesis with updated nuclear data. *Journal of Physics: Conference Series*, 202(1):012001, 2010.

[61] J. Dunkley et al. Five-Year Wilkinson Microwave Anisotropy Probe (WMAP) Observations: Likelihoods and Parameters from the WMAP data. *Astrophys.J.Suppl.*, 180:306–329, 2009.

[62] Alain Coc, Nelson J. Nunes, Keith A. Olive, Jean-Philippe Uzan, and Elisabeth Vangioni. Coupled Variations of Fundamental Couplings and Primordial Nucleosynthesis. *Phys.Rev.*, D76:023511, 2007.

[63] Christian M. Muller, Gregor Schafer, and Christof Wetterich. Nucleosynthesis and the variation of fundamental couplings. *Phys.Rev.*, D70:083504, 2004.

[64] Susana J. Landau, Mercedes E. Mosquera, Claudia G. Scoccola, and Hector Vucetich. Early Universe Constraints on Time Variation of Fundamental Constants. *Phys.Rev.*, D78:083527, 2008.

[65] Richard H. Cyburt, Brian D. Fields, Keith A. Olive, and Evan Skillman. New BBN limits on physics beyond the standard model from He-4. *Astropart.Phys.*, 23:313–323, 2005.

[66] Chung-Pei Ma and Edmund Bertschinger. Cosmological perturbation theory in the synchronous and conformal Newtonian gauges. *Astrophys.J.*, 455:7–25, 1995.

[67] R. Shankar. *Principles of Quantum Mechanics*. . Plenum Press, 1994.

[68] Sara Seager, Dimitar D. Sasselov, and Douglas Scott. A new calculation of the recombination epoch. *Astrophys.J.*, 523:L1–L5, 1999.

[69] P.J.E. Peebles. Recombination of the Primeval Plasma. *Astrophys.J.*, 153:1, 1968.

[70] James E. Gunn and Bruce A. Peterson. On the Density of Neutral Hydrogen in Intergalactic Space. *Astrophys.J.*, 142:1633, 1965.

[71] Elena Pierpaoli. Decaying particles and the reionization history of the universe. *Phys.Rev.Lett.*, 92:031301, 2004.

[72] Xue-Lei Chen and Marc Kamionkowski. Particle decays during the cosmic dark ages. *Phys.Rev.*, D70:043502, 2004.

[73] Nikhil Padmanabhan and Douglas P. Finkbeiner. Detecting dark matter annihilation with CMB polarization: Signatures and experimental prospects. *Phys.Rev.*, D72:023508, 2005.

[74] Tracy R. Slatyer, Nikhil Padmanabhan, and Douglas P. Finkbeiner. CMB Constraints on WIMP Annihilation: Energy Absorption During the Recombination Epoch. *Phys.Rev.*, D80:043526, 2009.

[75] J. Chluba. Could the Cosmological Recombination Spectrum Help Us Understand Annihilating Dark Matter? 2009.

[76] Douglas P. Finkbeiner, Silvia Galli, Tongyan Lin, and Tracy R. Slatyer. Searching for Dark Matter in the CMB: A Compact Parameterization of Energy Injection from New Physics. *Phys.Rev.*, D85:043522, 2012.

[77] Gaelle Giesen, Julien Lesgourgues, Benjamin Audren, and Yacine Ali-Haimoud. CMB photons shedding light on dark matter. 2012.

[78] J. M. Shull and M. E. van Steenberg. X-ray secondary heating and ionization in quasar emission-line clouds. *Astrophys.J.*, 298:268–274, November 1985.

[79] J. M. Shull. Heating and ionization by X-ray photoelectrons. *Astrophys.J.*, 234:761–764, December 1979.

[80] Steven Furlanetto and Samuel Johnson Stoever. Secondary ionization and heating by fast electrons. 2009.

[81] Silvia Galli, Rachel Bean, Alessandro Melchiorri, and Joseph Silk. Delayed Recombination and Cosmic Parameters. *Phys.Rev.*, D78:063532, 2008.

[82] A.H. Carter. *Classical and Statistical Thermodynamics*. Prentice Hall, 2001.

[83] Steven Furlanetto, S. Peng Oh, and Frank Briggs. Cosmology at Low Frequencies: The 21 cm Transition and the High-Redshift Universe. *Phys.Rept.*, 433:181–301, 2006.

[84] Marcos Valdes, Carmelo Evoli, Andrei Mesinger, Andrea Ferrara, and Naoki Yoshida. The nature of dark matter from the global high redshift HI 21 cm signal. 2012.

[85] Aravind Natarajan and Dominik J. Schwarz. Dark matter annihilation and its effect on CMB and Hydrogen 21 cm observations. *Phys.Rev.*, D80:043529, 2009.

[86] George F. Smoot, C.L. Bennett, A. Kogut, E.L. Wright, J. Aymon, et al. Structure in the COBE differential microwave radiometer first year maps. *Astrophys.J.*, 396:L1–L5, 1992.

[87] R. Durrer. *The Cosmic Microwave Background*. Cambridge University Press, 2008.

[88] James M. Bardeen. Gauge-invariant cosmological perturbations. *Phys. Rev. D*, 22:1882–1905, Oct 1980.

[89] Uros Seljak and Matias Zaldarriaga. A Line of sight integration approach to cosmic microwave background anisotropies. *Astrophys.J.*, 469:437–444, 1996.

[90] J.R. Bond and G. Efstathiou. Cosmic background radiation anisotropies in universes dominated by nonbaryonic dark matter. *Astrophys.J.*, 285:L45–L48, 1984.

[91] M. J. Rees. Polarization and Spectrum of the Primeval Radiation in an Anisotropic Universe. *ApJ*, 153:L1, July 1968.

[92] Yen-Ting Lin and Benjamin D. Wandelt. A Beginner's guide to the theory of CMB temperature and polarization power spectra in the line-of-sight formalism. *Astropart.Phys.*, 25:151–166, 2006.

[93] Matias Zaldarriaga and Uros Seljak. An all sky analysis of polarization in the microwave background. *Phys.Rev.*, D55:1830–1840, 1997.

[94] Marc Kamionkowski, Arthur Kosowsky, and Albert Stebbins. Statistics of cosmic microwave background polarization. *Phys.Rev.*, D55:7368–7388, 1997.

[95] Paolo Cabella and Marc Kamionkowski. Theory of cosmic microwave background polarization. 2004.

[96] Matias Zaldarriaga and Uros Seljak. Gravitational lensing effect on cosmic microwave background polarization. *Phys.Rev.*, D58:023003, 1998.

[97] S. Weinberg. *Cosmology*. Oxford University Press, 2008.

[98] Joseph Silk. Cosmic black body radiation and galaxy formation. *Astrophys.J.*, 151:459–471, 1968.

[99] John Kovac, E.M. Leitch, C Pryke, J.E. Carlstrom, N.W. Halverson, et al. Detection of polarization in the cosmic microwave background using DASI. *Nature*, 420:772–787, 2002.

[100] Diego Blas, Julien Lesgourgues, and Thomas Tram. The Cosmic Linear Anisotropy Solving System (CLASS) II: Approximation schemes. *JCAP*, 1107:034, 2011.

[101] Andrei Gruzinov and Wayne Hu. Secondary CMB anisotropies in a universe reionized in patches. *Astrophys.J.*, 508:435–439, 1998.

[102] Benjamin Audren, Julien Lesgourgues, Karim Benabed, and Simon Prunet. Conservative Constraints on Early Cosmology: an illustration of the Monte Python cosmological parameter inference code. 2012.

[103] C. Robert and G. Casella. *Monte Carlo Statistical Methods*. Springer Texts in Statistics. Springer, 2004.

[104] Roberto Trotta. Bayes in the sky: Bayesian inference and model selection in cosmology. *Contemp.Phys.*, 49:71–104, 2008.

[105] E. Komatsu et al. Seven-Year Wilkinson Microwave Anisotropy Probe (WMAP) Observations: Cosmological Interpretation. *Astrophys.J.Suppl.*, 192:18, 2011.

[106] Laurence Perotto, Julien Lesgourgues, Steen Hannestad, Huitzu Tu, and Yvonne Y.Y. Wong. Probing cosmological parameters with the CMB: Forecasts from full Monte Carlo simulations. *JCAP*, 0610:013, 2006.

[107] Fedor Simkovic, Rastislav Dvornicky, and Amand Faessler. Exact relativistic tritium beta-decay endpoint spectrum in a hadron model. *Phys. Rev.*, C77:055502, 2008.

[108] C.P. Burgess and G.D. Moore. *The standard model: a primer*. Cambridge University Press, 2007.

[109] D. Shiner, R. Dixson, and V. Vedantham. Three-nucleon charge radius: A precise laser determination using 3he. *Phys. Rev. Lett.*, 74(18):3553–3556, May 1995.

[110] G WF Drake, W Nortershauser, and Z C Yan. Isotope shifts and nuclear radius measurements for helium and lithium. *Canadian Journal of Physics*, 83(4):311–325, 2005.